

DISSERTATION

CHARACTERISTICS OF PRECIPITATION: CLOUDSAT OBSERVATIONS AND  
MODEL PREDICTIONS OF THE CURRENT AND FUTURE CLIMATE

Submitted by

Todd Douglas Ellis

Department of Atmospheric Science

In partial fulfillment of the requirements

For the degree of Doctor of Philosophy

Colorado State University

Fort Collins, Colorado

Summer 2008

UMI Number: 3332709

### INFORMATION TO USERS

The quality of this reproduction is dependent upon the quality of the copy submitted. Broken or indistinct print, colored or poor quality illustrations and photographs, print bleed-through, substandard margins, and improper alignment can adversely affect reproduction.

In the unlikely event that the author did not send a complete manuscript and there are missing pages, these will be noted. Also, if unauthorized copyright material had to be removed, a note will indicate the deletion.

**UMI**<sup>®</sup>

---

UMI Microform 3332709

Copyright 2008 by ProQuest LLC.

All rights reserved. This microform edition is protected against unauthorized copying under Title 17, United States Code.

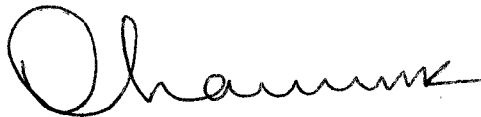
ProQuest LLC  
789 E. Eisenhower Parkway  
PO Box 1346  
Ann Arbor, MI 48106-1346

COLORADO STATE UNIVERSITY

July 8, 2008

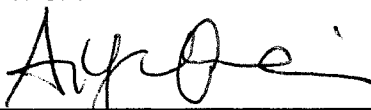
WE HEREBY RECOMMEND THAT THE DISSERTATION PREPARED  
UNDER OUR SUPERVISION BY TODD DOUGLAS ELLIS ENTITLED  
CHARACTERISTICS OF PRECIPITATION: CLOUDSAT OBSERVATIONS AND  
MODEL PREDICTIONS OF THE CURRENT AND FUTURE CLIMATE BE  
ACCEPTED AS FULFILLING IN PART REQUIREMENTS FOR THE DEGREE OF  
DOCTOR OF PHILOSOPHY.

Committee on Graduate Work



---

Dr. V. Chandrasekar



---

Dr. Aiguo Dai



---

Dr. Wayne H. Schubert



---

Dr. Graeme L. Stephens - Adviser



---

Dr. Richard H. Johnson - Department Head and  
Committee Member

## ABSTRACT OF DISSERTATION

### CHARACTERISTICS OF PRECIPITATION: CLOUDSAT OBSERVATIONS AND MODEL PREDICTIONS OF THE CURRENT AND FUTURE CLIMATE

The overall purpose of this study is to examine how the characteristics of precipitation are predicted by models to change in a typical climate change scenario, as well as to observe current characteristics of precipitation as they exist now and how well models reproduce those observations. The first part of this study examines the controls on global precipitation evident in transient experiments conducted using coupled climate models collected for the Intergovernmental Panel on Climate Change Fourth Assessment Report (IPCC AR4). The change in precipitation, water vapor, clouds, and radiative heating of the atmosphere evident in the 1% increase in carbon dioxide until doubled (1pctto2x) scenario are examined. As noted in other studies, the ensemble mean changes in water vapor as carbon dioxide increases to doubling occur at a rate similar to that predicted by the Clausius-Clapeyron relationship. This rate is more than three times the projected ensemble-mean sensitivity of precipitation to temperature change. A simple ratio of the precipitation sensitivity to water vapor sensitivity is introduced as a type of measure of the efficiency of the atmospheric branch of the global hydrological cycle in responding to changes in moisture. The value of this ratio varies between about 0.09 and 0.25 for the models studied. It is shown how increases in global precipitation track increases in atmospheric radiative energy loss and that the ratio of precipitation sensitivity to water vapor sensitivity is primarily determined by the rate at which the

emission of radiation from the clear-sky atmosphere, and consequently the surface warming, increases as water vapor increases. Furthermore, it is quantitatively shown that the magnitude of the efficiency ratio closely matches the sensitivity derived from simple energy balance arguments involving changes to water vapor emission alone by applying a square-root law model. Other factors that affect this efficiency include a negative cloud-radiation feedback associated with changes in the vertical distribution of clouds and a positive effect due to changes in sensible heating. While these factors individually are significant, they largely compensate for one another. These results are shown to cast some doubt on the state of observational studies that suggest larger rates of change in precipitation.

The second part of this study presents a new source of data that may address some of those observational concerns. The frequency of precipitation occurrence over the global oceans from 2006–2007 as calculated from CloudSat radar data is presented for the first time, showing structures of precipitation occurrence (rain and snow) into the high latitudes and calculating that precipitation occurs 11% of the time over the oceans. It is shown that the spatial pattern of the precipitation frequency from CloudSat is consistent with previous climatological studies. These data are verified through favorable comparisons to ship-based (ICOADS) and island-based (GSOD) data. The study then extends the use of these data to an analysis of the observed cloud structures that are associated with rainfall over the oceans and comparing that analysis to the state-of-the-art ECMWF weather forecast and HadGAM1 climate prediction models. These comparisons show that the ECMWF model appears to perform well, though it does not appear to

capture precipitation from shallow precipitation modes in the central Pacific, the HadGAM1 model grossly over produces rain globally nearly twice as often, and both models do not predict layered high clouds over precipitating low and mid-level clouds as often as they are observed by CloudSat.

Todd Douglas Ellis  
Department of Atmospheric Science  
Colorado State University  
Fort Collins, CO 80523  
Summer 2008

## ACKNOWLEDGMENTS

There are several groups to whom special thanks are owed for their assistance on this study. First of all, the author wishes to thank the numerous groups who made their data available for analysis. These include the groups who made their GCM data available to the Programme for Climate Model Diagnosis and Intercomparison (PCMDI), as well as to that organization for collecting and archiving those data for the CMIP3 study and the WCRP's Working Group on Coupled Modelling (WGCM) for organizing the data analysis activity. The WCRP CMIP3 multi-model dataset is supported by the Office of Science, U.S. Department of Energy. Another group worthy of special mention are Steve Worley, Scott Woodruff, Zaihua Ji and any others associated with the ICOADS project who rushed to make June and July 2007 data available for this study on special request. Special thanks also go out to Angela Benedetti of ECMWF and Alejandro Bodas-Salcedo of the Met Office for making their special model runs available for analysis. This analysis would have been impossible without their expertise. Finally, great thanks goes out to John Haynes, who has worked nonstop on perfecting his CloudSat precipitation retrieval while also juggling many other demands with grace.

The author would like to thank many people who have reviewed all or part of this work, including Graeme Stephens, Tristan L'Ecuyer, John Haynes, Paul Johnston, several anonymous reviewers, and of course, his committee, who have helped the author turn this dissertation around in short order and provided many useful comments during his defense.

This research has been supported in part by NASA Contract #NNG04GB97G, NASA CloudSat research grant #NNX07AR97G, and the U.S. Department of Energy Atmospheric Radiation Measurement program under Grant DE-FG03-94ER61748.

## DEDICATION

This dissertation could be dedicated to the many friends and family that have supported me and my growth and development over the years. It could also be dedicated to the many people who have suffered with me, either close by or from a distance as I struggled with the Ph.D. process. However, I must dedicate this to my wife and soul mate Allyson. She probably wishes that she had been a dissertation widow, but instead she was more of a personal 24/7 therapist. She has sacrificed a great deal more than she will probably ever let me know, and I am grateful that I have a lifetime to try to make it up to her.

## TABLE OF CONTENTS

ABSTRACT OF DISSERTATION.....	iii
ACKNOWLEDGMENTS.....	vi
DEDICATION.....	viii
TABLE OF CONTENTS.....	ix
LIST OF FIGURES.....	xii
LIST OF TABLES.....	xviii
CHAPTER 1: INTRODUCTION.....	1
1.1: Purpose of the study .....	1
1.2 Question I: How does the radiative budget of the atmosphere control changes to global precipitation?.....	4
1.3 Question II: What are the observed characteristics of precipitation and how well do models reproduce them?.....	6
1.4 The structure of this report.....	9
CHAPTER 2: Radiative controls of global-mean precipitation increases associated with climate change.....	10
2.1: Introduction.....	10
2.2: Data and methodology .....	14
2.3: Water vapor and precipitation changes in global warming simulations .....	16
2.4: Cloud and radiative heating changes in global warming simulations....	25

2.5: Global energy controls on precipitation.....	29
2.6: Summary and discussion.....	37
<b>CHAPTER 3: PRECIPITATION INCIDENCE FROM CLOUDSAT: VALIDATION AND MODEL EVALUATION .....</b>	<b>46</b>
3.1: Introduction.....	46
3.2: Data and Methodology.....	48
3.2.1: The CloudSat Precipitation Algorithm.....	48
3.2.2: The International Comprehensive Ocean-Atmosphere Data Set (ICOADS).....	50
3.2.3: Global Summary of the Day (GSOD) Station Data.....	52
3.2.4: The European Center for Medium-Range Weather Forecasting (ECMWF) Weather Forecast Model.....	54
3.2.5: The HadGAM1 Climate Configuration of the Met Office Unified Model.....	56
3.3: Results and discussion.....	57
3.3.1: Surface-based validation.....	57
3.3.2: CloudSat Precipitation Incidence.....	63
3.3.3: CloudSat and Model Comparison Study.....	70
3.4: Concluding remarks.....	82
<b>CHAPTER 4: CONCLUSIONS AND FUTURE WORK.....</b>	<b>86</b>
4.1: Summary of Conclusions.....	86
4.2: Questions for Future Study .....	88

CHAPTER 5: BIBLIOGRAPHY.....93

## LIST OF FIGURES

**Figure 2.1:** (a) The projected rate of relative percent change of column water vapor per degree increase of temperature amount derived from the Clausius-Clapeyron assuming the multi-model ensemble mean boundary layer temperature. Units are ( $\% \text{ K}^{-1}$ ). The global mean value of this sensitivity is  $6.7\% \text{ K}^{-1}$ . (b) The difference between the actual model projected rate of change of column water vapor and that derived from the Clausius-Clapeyron relationship as in Fig. 2.1a in units of ( $\% \text{ K}^{-1}$ ). (c) The change in ensemble mean winds from years 1-10 to years 61-70. Contours indicate changes in wind speed in ( $\text{m s}^{-1}$ ) and vectors represent the vector difference in winds at selected locations..... 18

**Figure 2.2:** (a) The absolute change in 1000-500 mb relative humidity (in %) from years 1-10 to years 61-70. (b) The absolute change in 0-500 mb relative humidity (in %) from years 1-10 to years 61-70. (c) The absolute change in precipitation rate (in  $\text{mm day}^{-1}$ ) from years 1-10 to years 61-70..... 21

**Figure 2.3:** The relative changes in column water vapor amount and precipitation rate, expressed as percentage changes, as functions of global temperature change derived from the AR4 models. The change in column water vapor derived assuming the C-C relationship (see text for explanation) corresponds to an increase of  $7.4\% \text{ K}^{-1}$ . The sensitivity of global precipitation rate changes to changes in temperature is approximately  $1.3\% \text{ K}^{-1}$ . The discrepancy between these two sensitivities indicates that the ratio of precipitation sensitivity to water vapor sensitivity in these models must be much less than unity. ....23

**Figure 2.4:** (a) The change in the global-mean precipitation efficiency as defined by the non-dimensionalized ratio of the precipitation sensitivity to the column water vapor sensitivity. (b) The global change in recycling or residence time for water vapor in the atmosphere in days, illustrating the slowing of the atmospheric branch of the hydrological cycle slows under global warming.....24

**Figure 2.5:** The changes in (a) low ( $p \geq 680$  mb), (b) mid-level ( $680 \text{ mb} > p \geq 440$  mb), and (c) high ( $p < 440$  mb) cloud amount (in percent) for selected models as indicated in Table 2.1.....27

**Figure 2.6:** The changes in (a) longwave, (b) shortwave, and (c) net cloud radiative forcing (in  $\text{W m}^{-2}$ ) for selected models as indicated in Table 2.1..... 28

**Figure 2.7:** The relationship between changes in latent heating ( $L \Delta P$ ) versus changes in atmospheric column cooling ( $\Delta R_{\text{net}}$ ) for the AR4 models. The dotted line represents the linear relationship between the two quantities, and the offset between that line and the solid line representing a one-to-one correspondence reflects the contribution of sensible heating to the energy balance.....31

**Figure 2.8:** A comparison of the model predicted precipitation efficiency  $\epsilon$  to estimates of the emission limit derived from changes in the radiative balance of model atmospheres for selected models. From left to right, the bars represent the water vapor emission limit based solely on changes in clear-sky column cooling for selected models, the predicted precipitation efficiency, the emission limit when including only the radiative effects of clouds, the emission limit when including only the effect of including sensible heating, and the emission limit when including both clouds and sensible heating. The ensemble

mean relationships appear in the rightmost set of bars. The error bars on the water vapor emission limit indicate the uncertainty in this limit due to uncertainty from the curve fit parameters  $b$  and  $c_o$  (see Table 2).....35

**Figure 2.9:** A summary of the key findings of this chapter. Absolute (Abs) changes in quantities (filled bars) correspond to the scale at the bottom of the figure and relative percentage (Rel) changes in quantities (hatched bars) refer to the scale at the top .....38

**Figure 3.1:** (a) Zonal mean annual mean precipitation incidence as reported by CloudSat for August 2006–July 2007 including only rain reports (circles) and both rain and snow reports (stars) compared against a range of values that represent the range of possible precipitation incidence values for that latitude band based on ICOADS ship reports for the same period, (b) The same but for DJF only, (c) MAM only, (d) JJA only, (e) SON only.....59

**Figure 3.2:** (a) Annual mean scatter plot of GSOD precipitation incidence (precip fraction) to the CloudSat precipitation incidence in the 2.5x2.5 degree boxes surrounding those stations. The thin solid line represents a slope of one, and the thick solid line flanked by dotted lines represents the best fit through zero for the data. The slope of this fit is  $0.80 \pm 0.04$ ., (b) The same as (a), but for the DJF season, with a fit of  $0.78 \pm 0.04$ , (c) MAM, fit is  $0.81 \pm 0.04$ , (d) JJA, fit is  $0.84 \pm 0.05$ , (e) SON, fit is  $0.87 \pm 0.05$ ..... 61

**Figure 3.3:** (a) Annual mean frequency of precipitation incidence as observed by CloudSat for the period of August 2006–July 2007. (b) Zonal mean frequency of

precipitation incidence as observed by CloudSat for each individual season, illustrating the observed seasonal cycle of precipitation incidence..... 64

**Figure 3.4:** The CloudSat observed relative frequency of occurrence of the cloud height of the lowest cloud layer when precipitation is detected (CTL) in June–August 2007, broken down by three ranges of heights: (a) low clouds (less than 4.75 km), (b) mid-level clouds (between 4.75 km and 11 km), and (c) high clouds (greater than 11 km). The deepest shade of red indicates a frequency of 1.0.....67

**Figure 3.5:** The CloudSat observed relative frequency of occurrence of the cloud height of the highest cloud layer when precipitation is detected (CTH) in June–August 2007, broken down by three ranges of heights: (a) low clouds (less than 4.75 km), (b) mid-level clouds (between 4.75 km and 11 km), and (c) high clouds (greater than 11 km). The deepest shade of red indicates a frequency of 1.0.....68

**Figure 3.6:** Regional breakdown of the relative frequency of occurrence of different cloud top heights for precipitation scenes. The left most set of bars represents the fraction of clouds below 4.75 km (low clouds), the middle set of bars represents the mid-level cloud top heights (4.75–11 km), and the right most set of bars represents high cloud top heights (above 11 km). In each set, the different shades distinguish between the CloudSat observed clouds and the ECMWF and HadGAM1 predict cloud distributions. The regions are defined in Table 3.2. (a) The relative frequency of cloud top height of the lowest detected cloud (CTL), which is presumably the cloud producing the surface precipitation. (b) The relative frequency of occurrence of the highest cloud top in the area (CTH). See text for more discussion..... 71

**Figure 3.7:** The ECMWF predicted relative frequency of occurrence of the cloud height of the lowest cloud layer when precipitation is detected (CTL) broken down by three ranges of heights: (a) low clouds (less than 4.75 km), (b) mid-level clouds (between 4.75 km and 11 km), and (c) high clouds (greater than 11 km). The deepest shade of red indicates a frequency of 1.0..... 75

**Figure 3.8:** The HadGAM1 predicted relative frequency of occurrence of the cloud height of the lowest cloud layer when precipitation is detected (CTL) broken down by three ranges of heights: (a) low clouds (less than 4.75 km), (b) mid-level clouds (between 4.75 km and 11 km), and (c) high clouds (greater than 11 km). The deepest shade of red indicates a frequency of 1.0.....76

**Figure 3.9:** The ECMWF predicted relative frequency of occurrence of the cloud height of the highest cloud layer when precipitation is detected (CTH) broken down by three ranges of heights: (a) low clouds (less than 4.75 km), (b) mid-level clouds (between 4.75 km and 11 km), and (c) high clouds (greater than 11 km). The deepest shade of red indicates a frequency of 1.0..... 78

**Figure 3.10:** The HadGAM1 predicted relative frequency of occurrence of the cloud height of the highest cloud layer when precipitation is detected (CTH) broken down by three ranges of heights: (a) low clouds (less than 4.75 km), (b) mid-level clouds (between 4.75 km and 11 km), and (c) high clouds (greater than 11 km). The deepest shade of red indicates a frequency of 1.0.....79

**Figure 3.11:** A comparison of the global maps of precipitation incidence from the three platforms used in this study. (a) The precipitation incidence from July–August 2007 as

observed by CloudSat (also Figure 3.3a); (b) The precipitation incidence from July–  
August 2007 as predicted by the ECMWF IFS; (c) The precipitation incidence as  
averaged over 5 consecutive JJA seasons by the HadGAM1 climate model.....83

## LIST OF TABLES

<b>Table 2.1:</b> PCMDI AR4 model simulations for which data were available used in this analysis. Asterisks indicate that the model was used for the emission limit analyses of Sections 2.5 and 2.6.....	15
<b>Table 2.2:</b> Retrieved parameters of the curve fit to the clear-sky atmospheric emission vs. column water vapor curves. Sigma represents the standard deviation in the parameters as returned from the curve fitting routine. Models not appearing on this list either had insufficient data for calculation or the curve fit did not converge to a physically reasonable value.....	33
<b>Table 3.1:</b> WMO present weather codes (“ww”) used to classify ICOADS precipitation events as possibly or certainly detectable by CloudSat. See Dai [2001a] for more details on these codes.....	52
<b>Table 3.2:</b> Selected regions for comparison as well as observed and predicted values of precipitation incidence (PI) for each region and platform.....	72

# **Chapter 1: Introduction**

## **1.1 Purpose of the Study**

Anthropogenically-forced climate change has emerged as perhaps the leading international environmental concern due to the potential economic, political, and societal ramifications it may hold. As scientists strive to understand this phenomenon, so too is society studying the importance of examining how such climate change could affect both developed and developing countries alike. It is telling that the 2007/8 United Nations Development Programme Human Development Report focused solely on the potential and current impacts of climate change on efforts to achieve sustainable development around the world [UNDP 2007]. In their announcement, they stress that “climate change is the greatest challenge facing humanity at the start of the 21st Century. Failure to meet that challenge raises the spectre of unprecedented reversals in human development.” Certainly, this underscores the urgency with which the scientific community must seek to understand both the causes and potential consequences of this phenomenon.

Policy makers around the world are indeed reacting now to meet the challenge that the UNDP raises. For example, in remarks surrounding the release of the Intergovernmental Panel on Climate Change (IPCC) Fourth Assessment Report (AR4), United Nations Secretary-General Ban Ki-Moon called climate change “the defining challenge of our age” and called on world leaders to be more constructive in upcoming

treaty meetings on carbon emissions [*New York Times*, 18 November 2007]. Perhaps there can be no greater acknowledgment of this assessment than the recognition of the former Vice President Albert Gore, Jr. and the IPCC with the 2007 Nobel Peace Prize. Yet, in order for policy makers to adequately address these challenges, science must continue to provide them with the information needed to assess not only the causes, but also the potential impacts of climate change.

Before this decade, most studies of anthropogenically-forced climate change have understandably focused on the impacts of climate change on the temperature record. Global warming, which has been reported by the IPCC as  $0.74^{\circ}\text{C} \pm 0.18^{\circ}\text{C}$  degrees of warming over the past 100 years [Trenberth et al., 2007b], is perhaps easier to understand than other potential impacts of climate change because it is a continuous state variable of the atmosphere and because improvements in measurement and interpolation techniques reduced the uncertainty in observations [Trenberth et al., 2007b]. Furthermore, the temperature record [e.g. Folland and Parker 1995], or proxies for the temperature record [e.g. Mann and Jones, 2003], are long in duration and therefore viable for the testing of trends that span decades and centuries. And there are numerous theories, both simple and complex, that directly connect changing concentrations of greenhouse gases to changes in the surface temperature of the planet [e.g. North et al., 1981]. However, easy to measure and understand though they may be, changes in surface temperature are not necessarily the most vital consequence of climate change from a societal standpoint.

In the past decade, studies have increasingly focused on the effects of climate change on the hydrological cycle of the planet, particularly the atmospheric branch of the

cycle. This is an important development in the course of climate study because of the essential role that water plays in the existence of life on Earth as well as the relatively small amount of water vapor that exists in the atmosphere at any given time. Consider that water vapor makes up only one-tenth of one percent of fresh water and one-millionth of the total water on the planet according to the most recent estimates of the global water budget [Chahine 1992, Trenberth et al., 2007a]. Yet, it is this atmospheric water vapor that is the sole source of water available to fall as precipitation, and it has been shown that precipitation is likely to be significantly affected by anthropogenic climate change [e.g. Diaz et al., 1989, Dai et al., 1997, Allen and Ingram, 2002, Trenberth et al., 2007b and others]. Such studies of the effect of climate change on the atmospheric branch of the hydrological cycle will continue to grow in importance as humanity rapidly increases the demand that it places on its fresh water supplies [e.g. Clarke and King, 2004].

This purpose of this study is therefore to contribute to the existing body of work on how anthropogenically-forced climate change affects the atmospheric branch of the hydrological cycle by answering two main research questions:

- (i) How does the radiative energy budget of the atmosphere change and how do those changes control changes in global-mean precipitation?
- (ii) What are currently observed characteristics of precipitation, both globally and regionally, and are those characteristics reproduced by state of the art forecast and climate models?

The following sections will briefly provide background and motivation for each of these research questions.

## **1.2 Question I: How does the radiative budget of the atmosphere control changes to global precipitation?**

Representing the inherent spatial variability and character of precipitation in global climate models is fraught with many difficulties and the determination of where and how much it rains or snows continues to be one of the most difficult and pressing challenges confronting weather and climate prediction. Yet, despite these difficulties, there appear to be robust physical controls on the global hydrological cycle that provide a basis for forming gross expectations as to how the global precipitation might change in the context of climate change [e.g. Allen and Ingram, 2002; Held and Soden, 2006]. Modeling studies suggest that atmospheric moisture increases with warming at a rate of approximately  $7\% \text{ K}^{-1}$  primarily due to the Clausius-Clapeyron (C-C) relation [e.g. Trenberth et al., 2007b] and observations over oceans demonstrate a similar rate of change [e.g. Santer et al., 2007]. Although there is an expectation that precipitation too should increase at approximately the same rate [e.g. Wentz et al., 2007], a number of studies, including the study presented in chapter two, point out that projected changes in precipitation by models occur at a much reduced rate of  $1\text{-}3\% \text{ K}^{-1}$ . Studies of Zhang et al., [2007], Wentz et al., [2007], and Allan and Soden [2007] appear to suggest that observations of precipitation change may, however, be more in line with the C-C implied moisture increase ( $7\% \text{ K}^{-1}$ ).

The current analysis further examines the controls on global precipitation evident in the transient experiments conducted using coupled climate models collected for the Intergovernmental Panel on Climate Change Fourth Assessment Report (IPCC AR4)

(<http://www.ipcc.ch>). The experiments analyzed are those of a 1% increase in carbon dioxide per year to doubling (also known as the 1pctto2x scenario). As has been known for some time [e.g. Stephens et al., 1994; Mitchell et al., 1987; Allen and Ingram, 2002; and others], global precipitation is constrained by changes in the energy balance of the atmosphere due to the radiative effects of increased water vapor more than it is by availability of moisture for conversion to precipitation. The model analysis presented in this study demonstrates that it is through this control that the rate of precipitation increase due to warming cannot be expected to keep pace with water vapor increases.

This study introduces a proximate measure of the efficiency of the atmospheric branch of the hydrological cycle given by the non-dimensional ratio of global-mean precipitation changes to global-mean water vapor changes. Using this ratio, it is shown that the rate at which radiation is emitted from the atmosphere by water vapor establishes a basic reference limit on this ratio with values that are substantially below that expected from the implied C-C increase in water vapor. It is further illustrated that the cloud-radiative feedbacks associated with changes in radiative heating related to changes in vertical cloud structure further reduces the ratio from the upper clear-sky emission limit and in this way acts as a negative feedback on global precipitation. These results raise questions about the aforementioned data sources used to infer observed changes in precipitation and the corresponding claim that the efficiency of the atmospheric branch of the hydrologic cycle should be near unity.

### **1.3 Question II: What are the observed characteristics of precipitation and how well do models reproduce them?**

Trenberth et al., [2003] correctly point out that as the climate changes, “the main changes in precipitation will likely be in the intensity, frequency, and duration of events, but these characteristics are seldom analyzed in observations or models.” To effectively analyze these characteristics, one must actually examine three related issues: observations of the current state of that variable, the accuracy with which the models reproduce those observations, and the nature of the predicted changes themselves. Examining these issues allows for a true assessment of the fidelity of the predictions, as a model that cannot accurately reproduce observations does not encourage confidence in its predictions. The first part of this study will have already addressed the nature of the predicted changes in precipitation. This second research question will attempt to address the other two issues through observing the incidence of precipitation and evaluating the accuracy of model reproductions of those observations.

Precipitation is notoriously difficult to observe due to both its high variability in both space and time as well as its spatial scale, which is typically smaller than those scales explicitly resolved by models of the climate. Even annual precipitation, which is adequately measured by rain gauge networks, is not well sampled over the ocean. These difficulties make it difficult to measure trends, frequency distributions, or even mean rainfall over global or regional scales. The recognition of these difficulties has long served as the motivation for developing satellite-based methods for observing the global distribution of precipitation [Stephens and Kummerow, 2007] and sustaining global-scale

observations over time scales relevant to climate change have not yet proven possible as evidenced in recent studies that report on contradictory long-term trends in existing satellite-based precipitation observations [e.g. Wentz et al., 2007, Gu et al., 2007]. Representing the inherent spatial variability and character of precipitation in global climate models is also fraught with many difficulties and the determination of where and how much it rains or snows continues to be one of the most difficult and pressing challenges facing climate prediction.

There have been several studies that have reported the characteristics of precipitation using the existing observational networks. For example, studies such as Dai [2001a,b] and Sun et al. [2007] have used surface-based observations to attempt to characterize important aspects of precipitation, such as global distributions of the precipitation incidence, numbers of days with rain, and the diurnal cycle, as well as rain rate (which represents the daily average rainfall) and rain intensity (which differs from the rain rate in that it is a conditional rate that discounts times when it is not raining). These types of observations are particularly important for understanding the nature of changes in precipitation frequency and intensity in climate change scenarios. Yet these studies, like many others, have been hampered by the dearth of surface-based precipitation data over the oceans, largely because even the most state-of-the-art oceanic surface based data [ICOADS, Worley et al., 2007] are necessarily tied to the shipping routes and the locations of buoys. In order to better understand global and regional precipitation, this difficulty needs to be overcome.

Rather than duplicate previous analyses of the characteristics of precipitation, this study seeks to make use of a new satellite-borne observing system to add to and hopefully improve upon the observations of how often precipitation occurs over the oceans. CloudSat [Stephens et al., 2002] is the first-ever spaceborne cloud radar, and since it became operational in 2006 it has provided the scientific community with unique, high-resolution observations of the structure of clouds worldwide. The data from CloudSat have proven to be quite useful for understanding cloud structure and properties, and have recently been extended to include a retrieval of precipitation incidence and intensity over the oceans [Haynes et al., 2008]. These data provide new insights into the characteristics of precipitation into the high latitudes as well as the types of cloud profiles associated with that precipitation.

This study therefore provides validation of the precipitation incidence portion of the CloudSat observations using well-established surface-based rainfall incidence data from the ICOADS and Global Summary of the Day [GSOD, Lott and Baldwin, 2002] datasets. These comparisons show that the CloudSat precipitation incidence data compare very favorably with both validation datasets and exhibit exceptional opportunities for analysis. As an example, in order to examine how well models reproduce the characteristics of clouds that produce precipitation, the validated results of CloudSat precipitation incidence and the relative frequency of occurrence of various cloud types are then used as a basis of comparison to special runs of the ECMWF IFS (<http://www.ecmwf.int>) weather model and the Met Office HadGAM1 climate model [Martin et al., 2006]. These model data include non-standard data on cloud top heights

associated with precipitation specifically provided for comparison against the cloud profiles as seen by CloudSat. This study will illustrate that, while the models perform well in some cases, they also have shortcomings that can be quite important. The ECMWF model is shown to underpredict the presence of shallow modes of precipitation in the tropical oceans, while the HadGAM1 model greatly overestimate the occurrence of precipitation globally, and neither model adequately predicts the presence of high cloud over precipitating low clouds.

#### **1.4 The structure of this study**

The remainder of this study discusses these research questions in detail, including expanded background material, details on data used and research methods applied, results, and discussion. Chapter two presents a study of how changes in the radiative budget of the atmosphere constrain changes in the global-mean precipitation predicted by the same models. Chapter three presents a verification and analysis of CloudSat observations of precipitation incidence, as well as the comparison of those data to specially provided predictions from weather and climate models that give detailed information about the types of clouds present in each rainy scene. Chapter four provides a brief discussion of how the results of these studies provide a coherent picture of the nature of precipitation changes in these models and discusses research questions that arise from these results, Chapter five lists references that have been cited in this study.

# **Chapter 2: Radiative controls of global-mean precipitation increases associated with climate change**

## **2.1 Introduction**

Scientific discussion about long term climate change induced by the build up of greenhouse gases has predominantly focused on global warming. Although there remains much uncertainty on predictions of how much warming will occur through greenhouse gas build up, the predominant public focus on global surface temperature as a metric of climate change is in part understandable given that theories both simple and complex exist that directly connect perturbations of radiative forcing associated with changing concentrations of greenhouse gases to global-mean surface temperature [e.g. North et al., 1981]. Relatively long records of global surface temperature [Folland and Parker, 1995], or proxies for it [Mann and Jones, 2003], can also be constructed from diverse observations to provide a way of testing such theories. Changes to the characteristics of rainfall on both global and regional scales have recently been undergoing similar levels of scrutiny [e.g. Diaz et al., 1989; Dai et al., 1997; Allen and Ingram, 2002; Trenberth et al., 2007b] as the societal impacts of changes in precipitation have become more apparent [e.g. UNDP, 2007]. Understanding how precipitation patterns and types are likely to change in the face of increasing carbon dioxide [e.g. Trenberth et al., 2003] as well as by

other anthropogenic factors like pollution, are essential for understanding the scope of a looming planetary-scale water supply crisis [Clarke and King, 2004].

Precipitation is highly variable over both space and time and forms inherently on scales typically much smaller than those resolved explicitly by existing models of the Earth's climate. Even annual precipitation, which is adequately measured by existing land-based rain gauge networks, is not well sampled over the ocean. These difficulties create great problems for measuring global and regional-scale precipitation and major challenges for determining climate trends. The recognition of these problems has long served as motivation for the development of satellite-based methods for observing the global distribution of precipitation. Measurement of precipitation from space however is challenging [Stephens and Kummerow, 2007] and sustaining global-scale observations over time-scales relevant to the climate change problem has not yet proven possible as evidenced in recent studies that report on contradictory global trends in existing satellite-based precipitation observations [Wentz et al., 2007; Gu et al., 2007]. Representing the inherent spatial variability and character of precipitation in global climate models is also fraught with many difficulties and the determination of where and how much it rains or snows continues to be one of the most difficult and pressing challenges confronting weather and climate prediction.

Despite the difficulties associated with modeling, observing, and predicting changes in local and global-scale precipitation, there appear to be robust physical controls on the global hydrological cycle that provide a basis for forming gross expectations as to how the global precipitation might change in the context of climate change [e.g. Allen

and Ingram, 2002; Held and Soden, 2006]. Modeling studies suggest that atmospheric moisture increases with warming at a rate of approximately  $7\% \text{ K}^{-1}$  primarily due to the Clausius-Clapeyron (C-C) relation [e.g. Trenberth et al., 2007b] and observations over oceans demonstrate a similar rate of change [e.g. Santer et al., 2007]. Although there is an expectation that precipitation too should increase at approximately the same rate [e.g. Wentz et al., 2007], a number of studies including the present study point out that projected changes in precipitation by models occur at a much reduced rate ( $1\text{-}3\% \text{ K}^{-1}$ ). Studies of Zhang et al. [2007], Allan and Soden [2007], and Lambert et al. [2008] appear to suggest that observations of precipitation change may, however, be more in line with the C-C implied moisture increase ( $7\% \text{ K}^{-1}$ ).

This chapter further examines the controls on global precipitation evident in the transient experiments conducted using coupled climate models collected for the Intergovernmental Panel on Climate Change Fourth Assessment Report (IPCC AR4) ([www.ipcc.ch](http://www.ipcc.ch)). The experiments analyzed are those of a 1% increase in carbon dioxide per year to doubling. As has been known for some time [e.g. Stephens et al., 1994; Mitchell et al., 1987; Allen and Ingram, 2002; and others] global precipitation is constrained by the energy balance of the atmosphere more so than by availability of moisture and the model analysis presented in this study demonstrates that it is through this control that the rate of precipitation increase in warming cannot be expected to keep pace with water vapor increases. This result thus raises questions about the aforementioned data sources used to infer observed changes in precipitation.

The model data used in this study are briefly described in the following section together with the simple procedures developed for analysis of these data. Section 2.3 reviews the changes to column water vapor associated with the resultant global warming of the models offering a context for the following analysis. A non-dimensional ratio of the changes in global-mean precipitation to changes in global-mean water vapor is introduced in this section. This ratio,  $\epsilon$ , serves as a proxy for global precipitation efficiency, since it is a measure of how much the predicted increase in water vapor is converted to increased precipitation. Section 2.4 then reviews the changes in cloud amount that relate to the moisture changes described in section 2.3. The associated changes in atmospheric cloud radiative heating are also introduced in section 2.4 and it is shown how these changes are related to changes in the vertical structure of clouds with decreased middle level and low clouds and slightly increased high clouds producing the predicted heating. Section 2.5 examines the basic energy controls on the model hydrological cycle formulated in terms of the  $\epsilon$  ratio introduced in section 2.3. This section shows that the rate at which radiation is emitted from the atmosphere by water vapor establishes a basic reference limit on this ratio with values that are substantially below that expected from the implied C-C increase in water vapor. This section further illustrates how the cloud-radiative feedbacks associated with changes in radiative heating related to changes in vertical cloud structure further reduces the ratio from the upper clear-sky emission limit and in this way acts as a negative feedback on global precipitation. The chapter concludes with a discussion of these results that appear to

contradict the recent observational studies that suggest a value of  $\epsilon$  ought to be nearly unity.

## 2.2 Data and methodology

The data used in this study are those of coupled climate models archived by the World Climate Research Programme's (WCRP's) Coupled Model Intercomparison Project phase 3 (CMIP3) multi-model data set (<http://www-pcmdi.llnl.gov/>) [Meehl et al., 2007]. The focus of this particular study is directed toward addressing the nature of changes that occur under predicted global warming due to a 1% per year increase in carbon dioxide over 70 years from present at which point in time  $\text{CO}_2$  is doubled from initial levels (referred to by PCMDI as the 1pctto2x scenario). This permits the study of the differences in the hydrological cycle before and after the carbon dioxide change. It also makes possible a study of the evolution of the system in order to shed more light on the physical mechanisms involved. For this analysis, only one realization from each of 21 models (listed in Table 2.1) is considered<sup>1</sup>. It is important to note that not all models contribute to all calculated quantities studied in this paper when relevant data are missing. These missing data also limit on the number of models that can be used for the analysis in Section 2.5. In order to obtain self-consistent results, only 7 models, highlighted with an asterisk in Table 2.1, are used in those analyses since they were the only models to have available, realistic data for each field necessary to calculate clear-sky and all-sky column radiative energy fluxes as well as cloud-radiative forcing fluxes.

---

<sup>1</sup> Run 1 is used in all cases except for the NCAR-PCM1 model where Run 2 is used because it includes an entire model integration in one file

Model	Country	Model	Country
BCC CM1	China	IPSL CM4*	France
BCCR BCM2.0	Norway	MIROC HiRes*	Japan
CCCMA CGCM3.1*	Canada	MIROC ModRes*	Japan
CNRM CM3	France	MIUB ECHO-G	Germany/Korea
CSIRO MK3.0	Australia	MPI ECHAM5	Germany
GFDL CM2.0*	United States	MRI CGCM 2.3.2A	Japan
GFDL CM2.1*	United States	NCAR CCSM3	United States
GISS EH	United States	NCAR PCM1	United States
GISS ER	United States	UKMet HadCM3	United Kingdom
IAP FGOALS	China	UKMet HadGem1	United Kingdom
INMCM 3.0*	Russia		

Table 2.2: PCMDI AR4 model simulations for which data were available used in this analysis. Asterisks indicate that the model was used for the emission limit analyses of Sections 2.5 and 2.6

The analyses of this study consider averages over years 1-10 and 61-70 in order to mitigate contributions of year-to-year variability. Differences between these averages illustrate how the atmospheric states change from initial values as the models approach a doubling in carbon dioxide concentrations. In order to present robust geographical responses of models, maps of the ensemble means of data exclude values outside of one standard deviation to remove possible effects of model outliers. The responses presented, however, do not change significantly when values within two standard deviations of the mean are included (not shown). Finally, globally averaged quantities are derived using appropriate equal area weighting of model grid point data.

## 2.3 Water vapor and precipitation changes in global warming simulations

In studying the factors that control precipitation changes in global warming it is relevant to first consider changes to water vapor for context. The following simplistic arguments illustrate how precipitation changes might relate to the water vapor increases that are uniformly predicted by the climate models considered in this study. It is commonly argued that precipitating weather systems of all kinds feed mostly on the moisture that already resides in the atmosphere [e.g. Trenberth, 1998], primarily through low-level convergence of this moisture in the vicinity of weather systems. Therefore changes to the availability of atmospheric moisture, through projected water vapor increases due to global warming, can be expected to lead directly to changes in this moisture convergence and hence precipitation intensity. It is through these arguments that the rate of precipitation increase might follow the rate of water vapor increase.

The Clausius-Clapeyron (hereafter C-C) relationship for saturated vapor pressure presents a much-discussed basis for understanding the predicted changes to atmospheric water vapor under global warming. This relationship is given by:

$$\frac{d \ln e_s}{dT_s} = \frac{L}{RT_s^2} \quad (2.1)$$

where  $L$  is the latent heat of vaporization,  $R$  is the gas constant and  $e_s$  is the saturation vapor pressure at the surface associated with the surface temperature  $T_s$ . It has been assumed for some time that the column total water vapor in the atmosphere follows the behavior expected from this relationship. This expectation is confirmed in the study of

Stephens [1990] and others [e.g. Wentz and Schabel, 2000; Trenberth et al., 2005] through analysis of satellite data. Many other studies [e.g. Held and Soden, 2006] also underscore this key point by arguing that the changes in column mean water vapor under global warming closely follow a projected C-C increase of approximately  $7\% \text{ K}^{-1}$  given the associated increase in surface temperature.

Figure 2.1 offers a closer examination of the relationship between the column water vapor predicted from the C-C relationship and the model predicted water vapor. Figure 2.1a presents the global distribution of the percentage increase in water vapor per degree warming calculated from the C-C relation using ensemble-mean model surface to 700 hPa mean layer temperature averaged over the first 10 years of integration. This layer mean temperature is taken to characterize the boundary layer temperature where most of the water vapor resides and thus is broadly characteristic of the column water vapor (CWV). The global-mean value of the fractional rate of increase of water vapor calculated using layer mean temperatures is  $6.7\% \text{ K}^{-1}$ . Calculated in this way, the results of this figure can be interpreted as representing the contribution to the rate of increase of model water vapor per degree warming that would occur purely through thermodynamic controls on water vapor under the common assumption that relative humidity remains fixed. This assumption of fixed relative humidity is validated by the results of Dai [2006], among others.

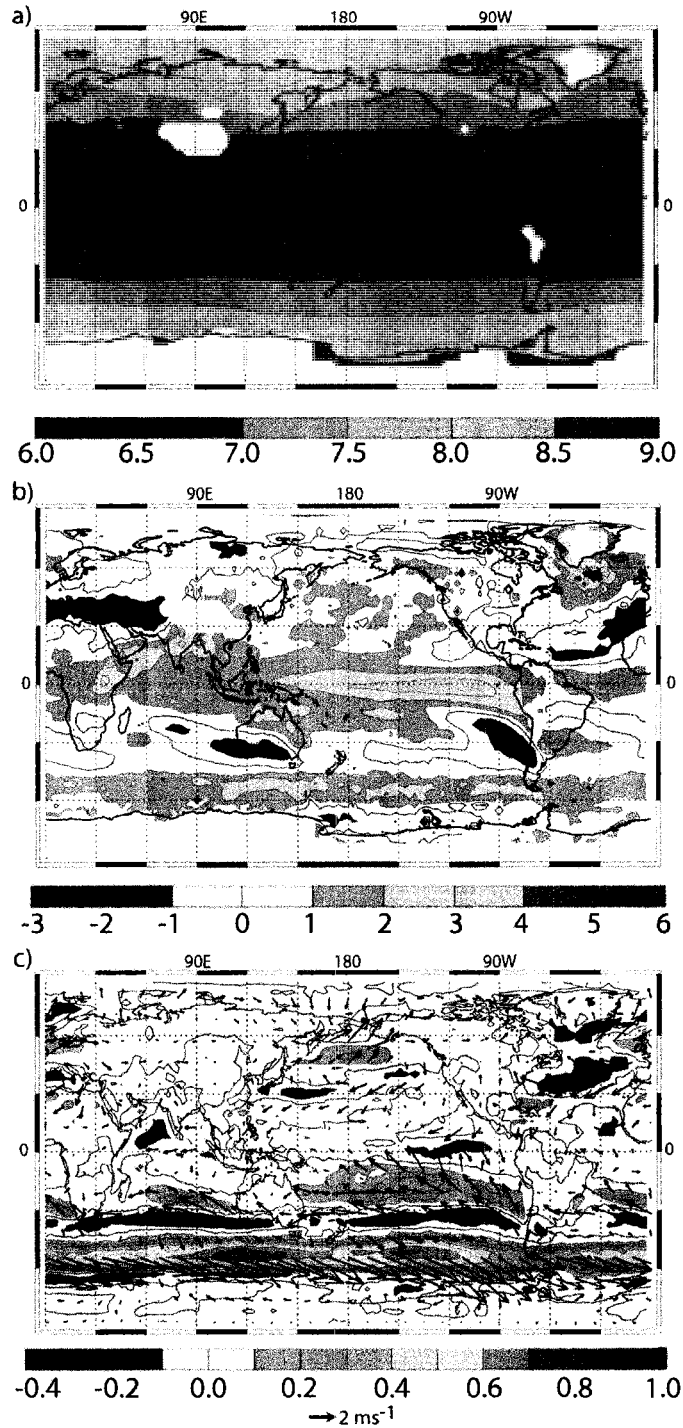


Figure 2.1: (a) The projected rate of relative percent change of column water vapor per degree increase of temperature amount derived from the Clausius-Clapeyron assuming the multi-model ensemble mean boundary layer temperature. Units are (% K<sup>-1</sup>). The global mean value of this sensitivity is 6.7% K<sup>-1</sup>. (b) The difference between the actual model projected rate of change of column water vapor and that derived from the Clausius-Clapeyron relationship as in Fig. 2.1a in units of (% K<sup>-1</sup>). (c) The change in ensemble mean winds from years 1-10 to years 61-70. Contours indicate changes in wind speed in (m s<sup>-1</sup>) and vectors represent the vector difference in winds at selected locations.

A similar quantity to that of Fig. 2.1a can also be derived from the ensemble mean of the ratio of model-predicted column water vapor changes divided by the respective surface temperature increases of each model. The difference between this sensitivity and that derived from C-C is shown in Fig. 2.1b. It reveals how most models moisten over oceans at rates that slightly exceed the simple thermodynamic increase as embodied in the C-C relationship, and that this enhanced moistening is substantial in some regions. Differences between real-world observed water vapor and water vapor derived from this specific form of the C-C relationship reveal atmospheric circulation influences on water vapor [Stephens, 1990]. In an analogous way, the differences shown in Fig. 2.1b reveal the influence of changes in the atmospheric circulation on the model water vapor increases. To underscore this point, Fig. 2.1c shows the model ensemble mean changes in surface wind speed and velocity (arrows). It suggests that the increased mid-latitude westerlies over the southern oceans poleward of about 40° S drive the increased water vapor through evaporation associated with these stronger winds. The extensive area of enhanced moistening over the tropical Pacific ocean appears to be related to enhanced moisture convergence into this region. These results are also consistent with Vecchi and Soden [2007], who show that these regions of moistening beyond that predicted by the C-C relation are also regions where the vertical velocity is changing in connection to a weakening of the tropical Walker circulation<sup>2</sup>.

---

<sup>2</sup> Vecchi and Soden (2007) study the changes in the SRES A1B scenario of the IPCC AR4 models. This corresponds to a doubling of equivalent carbon dioxide between 2000 and 2100, after which time the radiative forcings are held constant.

The global and ensemble mean sensitivity of the AR4 models is  $7.4\% \text{ K}^{-1}$ , which slightly exceeds that derived from C-C as shown in Fig. 2.1a ( $6.7\% \text{ K}^{-1}$ ) implying a modest change in relative humidity in the models. It is usually assumed that the relative humidity changes that occur in climate change are small and that on the whole the water vapor feedback in models is interpreted through a mechanism that inherently is structured around assumptions of fixed relative humidity. However, the potential importance of even these small changes to relative humidity are evident in Figs. 2.2a and 2.2b. The geographic changes in layer-mean surface to 500 hPa relative humidity (Fig. 2.2a) are small but nevertheless coherent in structure showing wide-scale decreases of relative humidity in the sub-tropics and increases in regions that could be anticipated from the difference maps of Fig. 2.1b. The increases are confined to the tropical regions and the mid-to-higher latitudes and decreases in relative humidity existing in broad regions of the subtropics and some regions of the tropical atmosphere. Figure 2.2b shows the changes in ensemble-mean relative humidity in the layer above 500 hPa. Increases in relative humidity of the upper troposphere are more broadly spread with largest increases coupled to regions of increased lower tropospheric relative humidity. Upper-tropospheric drying occurs in regions of the subtropics where increases to subsidence presumably occurs as found in Vecchi and Soden [2007].

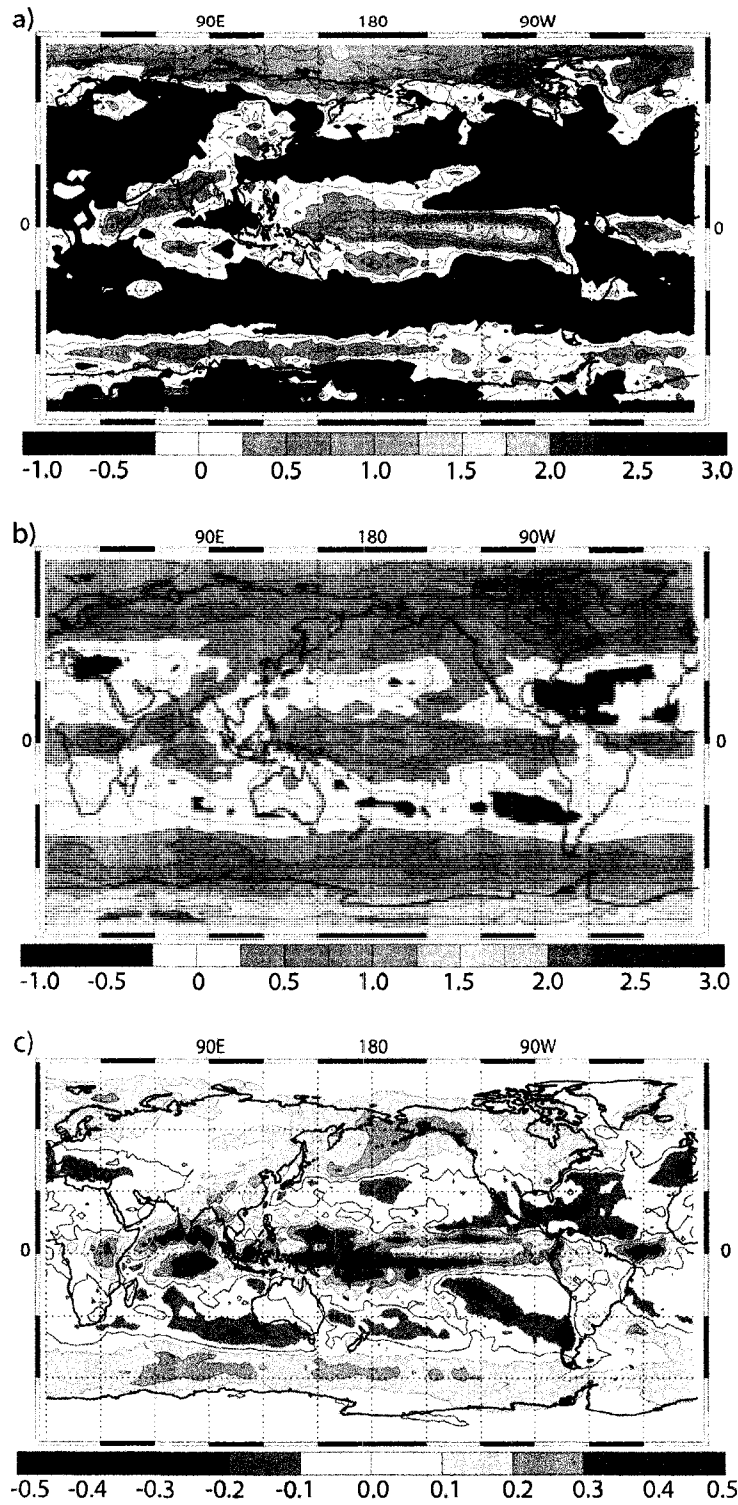


Figure 2.2: (a) The absolute change in 1000-500 mb relative humidity (in %) from years 1-10 to years 61-70. (b) The absolute change in 0-500 mb relative humidity (in %) from years 1-10 to years 61-70. (c) The absolute change in precipitation rate (in mm day<sup>-1</sup>) from years 1-10 to years 61-70.

Although the changes in relative humidity are small, they appear to exert an important influence on changes to the hydrological cycle. The ensemble-mean distribution of precipitation change is shown in Fig. 2.2c and comparison to Fig. 2.2a underscores how the distribution of precipitation change in the tropics and in the southern oceans, to a large degree, mirror the change in lower atmospheric relative humidity in these regions. However, the relationship between the precipitation changes and the relative humidity is not sufficient to wholly describe the model-simulated changes since climate change also includes an effect on the ratio of the global-mean precipitation sensitivity to the global-mean water vapor sensitivity. These changes, which represent a proxy for the efficiency of the global atmosphere's conversion of increased water vapor into increased precipitation, are explored below.

Figure 2.3 provides a slightly different perspective on the results of Fig. 2.1 by showing the differences in global-mean column water vapor,  $\Delta W$ , as a function of the global-mean surface temperature,  $\Delta T_s$ , for all models studied. In the previous section, it is noted that the global-mean sensitivity deduced from the individual models to be approximately  $7.4\% \text{ K}^{-1}$  slightly exceeding the C-C inferred global mean value by  $0.7\% \text{ K}^{-1}$ . Figure 2.3 also contrasts the change in precipitation as a function  $\Delta T_s$ . The sensitivity of precipitation to changes in surface temperature is approximately  $1.3\% \text{ K}^{-1}$  [also Held and Soden, 2006]. At this point, it is convenient to introduce the following non-dimensionalized ratio of the precipitation sensitivity to water vapor sensitivity, namely

$$\epsilon = \frac{W}{P} \frac{\Delta P}{\Delta W} \quad (2.2)$$

where  $W$  and  $P$  are global mean values of column water vapor and precipitation respectively and  $\Delta P$  and  $\Delta W$  are the increased precipitation and column water vapor related to global warming, respectively.

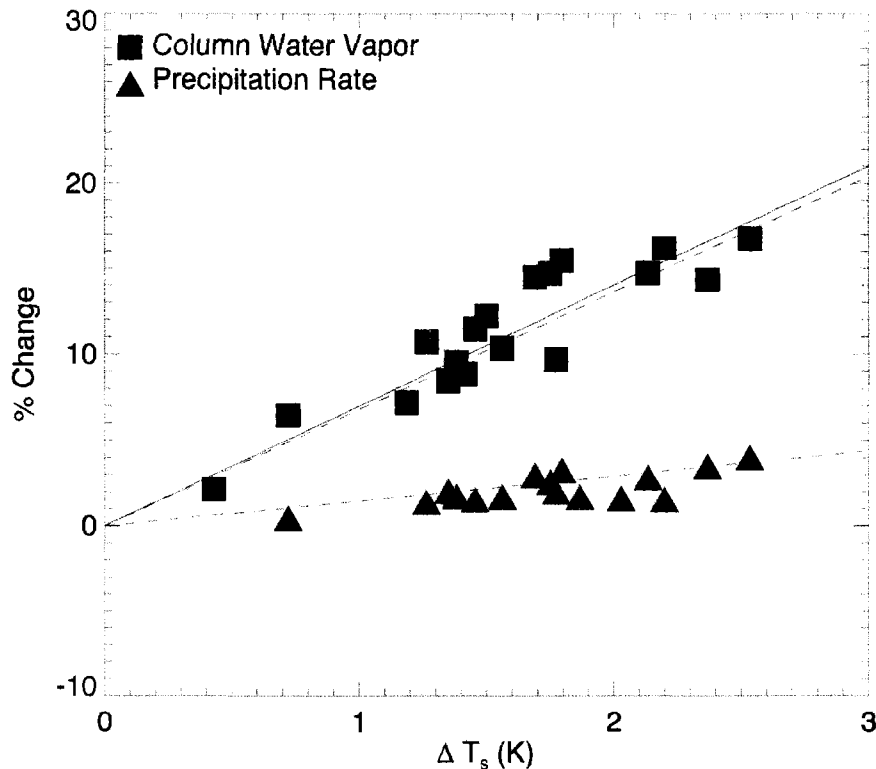


Figure 2.3: The relative changes in column water vapor amount and precipitation rate, expressed as percentage changes, as functions of global temperature change derived from the AR4 models. The change in column water vapor derived assuming the C-C relationship (see text for explanation) corresponds to an increase of 7.4 % K<sup>-1</sup>. The sensitivity of global precipitation rate changes to changes in temperature is approximately 1.3 % K<sup>-1</sup>. The discrepancy between these two sensitivities indicates that the ratio of precipitation sensitivity to water vapor sensitivity in these models must be much less than unity. Note: Not all models had both column water vapor and precipitation data.

This ratio is a simple proxy of the atmosphere's efficiency in converting increased global-mean water vapor into increased global-mean precipitation. It also provides a simple way of examining the disparity between the scaling of precipitation that might be expected

from C-C alone (hereafter  $\epsilon_{C-C} = 1$ ) and the actual changes predicted by models. Figure 2.4a shows this quantity for individual models indicating a range from 0.09 to 0.25, substantially below  $\epsilon_{C-C} = 1$ .

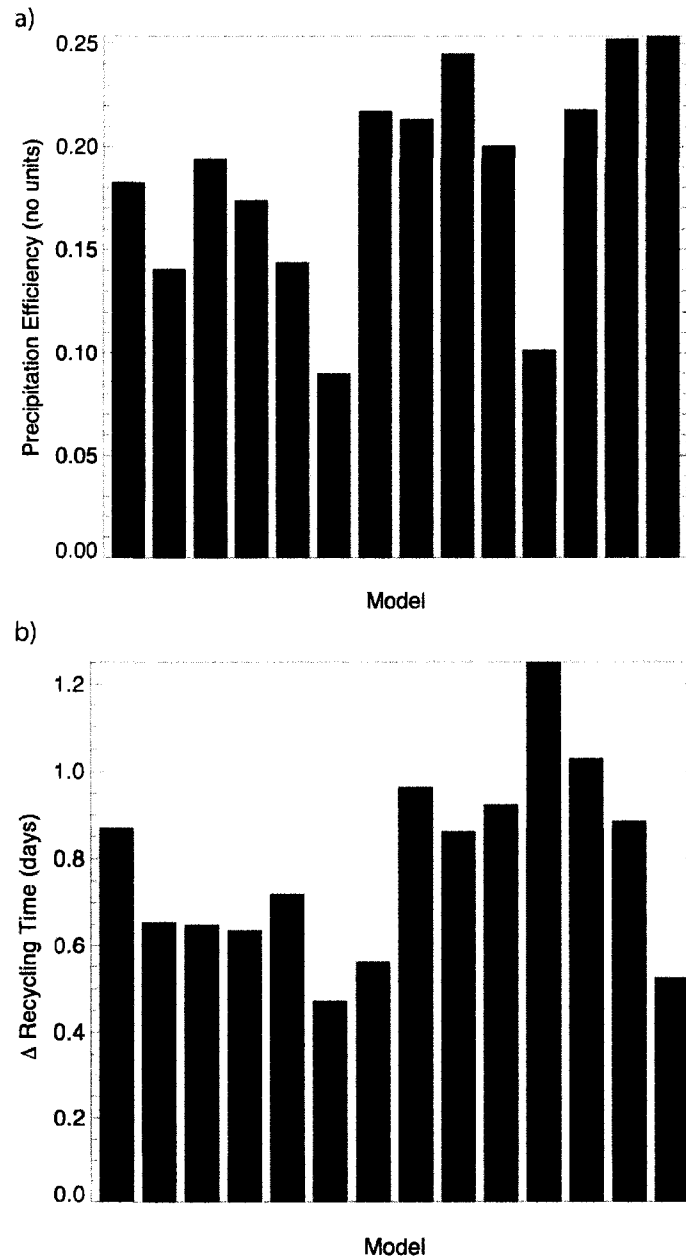


Figure 2.4: (a) The change in the global-mean precipitation efficiency as defined by the non-dimensionalized ratio of the precipitation sensitivity to the column water vapor sensitivity. (b) The global change in recycling or residence time for water vapor in the atmosphere in days, illustrating the slowing of the atmospheric branch of the hydrological cycle slows under global warming.

Since the time scale of the cycling of water in the atmosphere is also dictated broadly by the ratio of the total water vapor in the atmosphere to precipitation rate [e.g. Trenberth, 1998], then the reduced sensitivity of precipitation relative to the sensitivity of water vapor also implies that the time scale of cycling of water through the atmosphere must also be increased in these global warming experiments [Bosilovich et al., 2005]. This is confirmed in Fig. 2.4b showing the change in residence time of water vapor in the atmosphere. The reduced residence time, and thus the implied slowing of the atmospheric branch of the hydrological cycle, has been noted in other contexts such as in those studies that examine the change in the character of precipitation with more intense storms occurring in a warmed climate with longer periods between events [Tselioudis and Rossow, 2006; Kharin and Zwiers, 2005; Groisman et al., 2005]. Held and Soden [2006] also note how the model convective mass fluxes are also reduced under global warming and Vecchi and Soden [2007] outline changes in model predicted vertical velocity, both of which are also consistent with a slowing of this branch of the hydrological cycle.

## **2.4 Cloud and radiative heating changes in global warming simulations**

Figures 2.5 and 2.6 respectively show the changes in global cloud amount and atmospheric column radiative heating due to these cloud changes. These ensemble mean results include only the seven models indicated in Table 2.1. The pressure ranges defined by the International Satellite Cloud Climatology Project [ISCCP, Schiffer and Rossow, 1983] for high, middle and low cloud are also applied in this study. Figure 2.5 reveals small increases in high clouds over the eastern tropical Pacific and at higher latitudes and decreases in high clouds over a broad region centered on the maritime continent. There

are also small but wide spread decreases of low clouds between 30-60° N/S consistent with the slight decreases of relative humidity observed in the lower troposphere (Figure 2.2a). The largest changes in cloudiness, however, are the wide-scale decreases of mid-level clouds particularly in the mid-latitudes and over the maritime continent.

The changes in cloud vertical structure implied in the results of Figure 2.5 impose important influences on the radiative budget of the atmospheric column. This influence can be measured by the contribution of clouds to the column radiative heating as introduced by  $C_{net}$  in (2.5) below. Figure 2.6 presents  $C_{net}$  and the individual long and shortwave components that define it. The decreases in middle level clouds, and to a lesser extent lower clouds, induce a net column warming by proportionally exposing the higher clouds above to the warmer lower atmosphere. This results in a broad increase in the longwave contribution to  $C_{net}$ , especially in mid-latitudes where the heating pattern mirrors the pattern of change in mid-level clouds. A tongue of strong heating also exists over the tropical mid-to-eastern Pacific due to the small increases of high clouds.

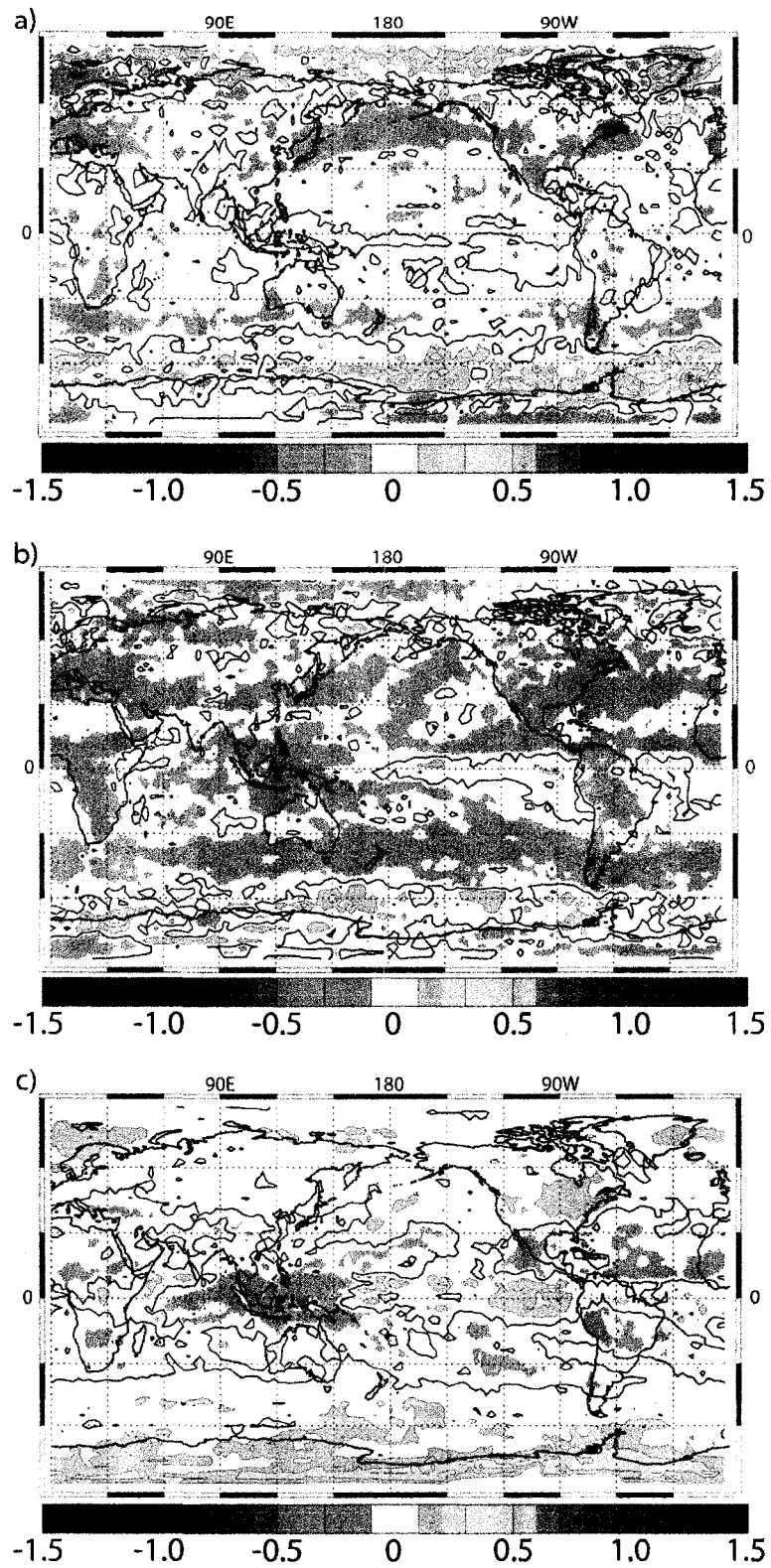


Figure 2.5: The changes in (a) low ( $p \geq 680$  mb), (b) mid-level ( $680 \text{ mb} > p \geq 440$  mb), and (c) high ( $p < 440$  mb) cloud amount (in percent) for selected models as indicated in Table 2.1.

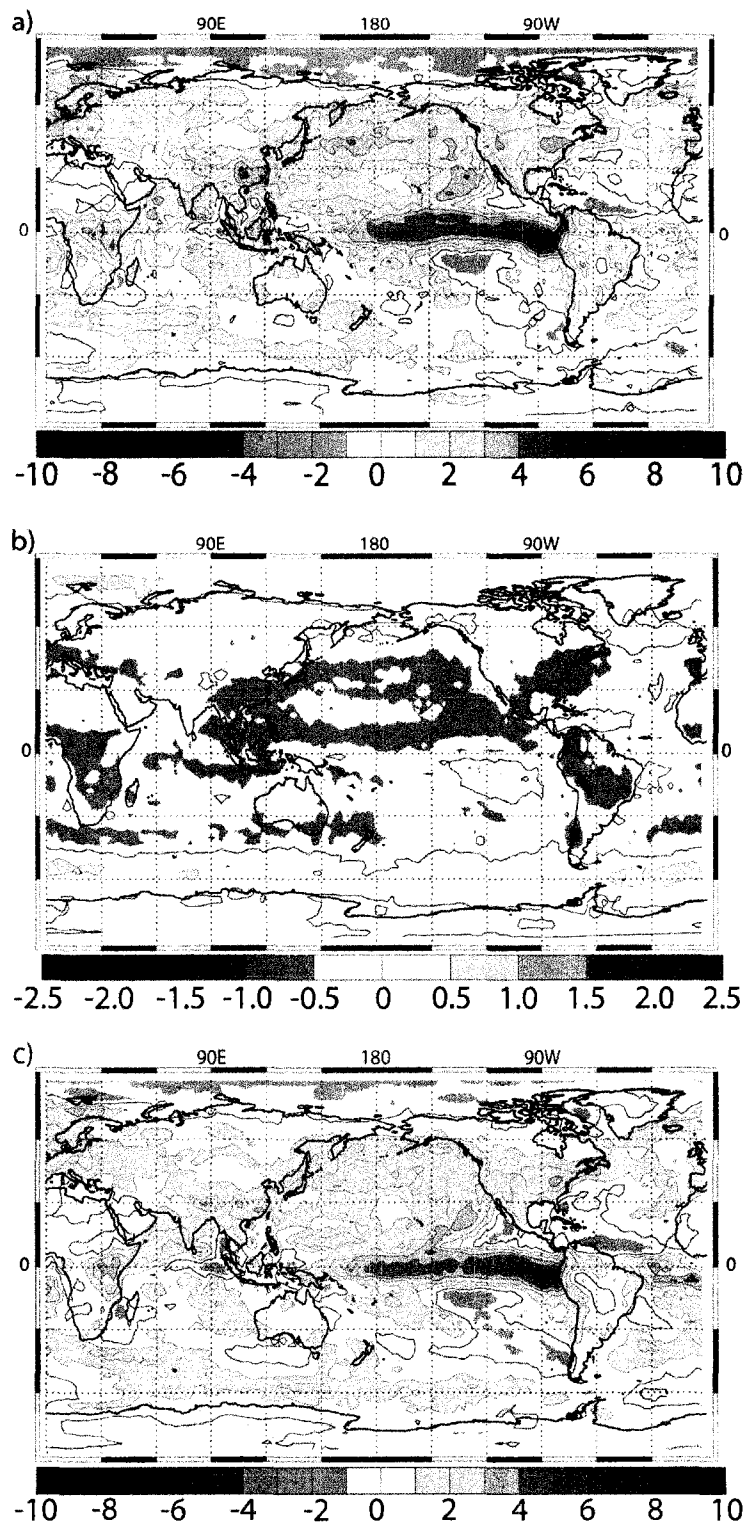


Figure 2.6: The changes in (a) longwave, (b) shortwave, and (c) net cloud radiative forcing (in  $\text{W m}^{-2}$ ) for selected models as indicated in Table 2.1.

## 2.5 Global energy controls on precipitation

It is obvious from the results of Figure 2.3 that more influential controls on global precipitation exist in models other than those of moisture availability alone. While the latter might influence regional changes in precipitation to some degree, as noted in comparison of the changes to low level relative humidity (Figure 2.2a) and precipitation (Figure 2.2c), increased water vapor governs the changes to global precipitation in a more indirect but significant way. As noted earlier, it has been understood for some time that the global hydrological cycle and global atmospheric energy budget are intimately linked and that changes to atmospheric energy, more so than changes to water variability, control the hydrological cycle on the global scale [Stephens et al., 1994; Stephens, 2005; Mitchell et al., 1987; Allen and Ingram, 2002].

This energy-based control is now examined in the context of the ratio  $\epsilon$  introduced in Section 2.3. First, consider the atmospheric energy balance of the form

$$\Delta R_{net,atm} = S + LP \quad (2.3a)$$

where  $R_{net,atm}$  is the net radiative energy loss from the atmosphere that occurs as a result of the fact that emission of radiation from the atmosphere exceeds absorption of radiation by the atmosphere. This net radiative loss is balanced by the input of energy from convective processes that transport both sensible ( $S$ ) and latent ( $LP$ ) heat from the surface and deposit it in the atmosphere where  $P$  is the surface precipitation and  $L$  is the latent heat of vaporization. In general, the larger of these two turbulent contributions is the latent heating associated with evaporation of water from the surface, mostly over the world's oceans. This simple balance between radiation losses and heat added from the

surface and mixed into the atmosphere by convection constitutes a general state of radiative convective equilibrium [e.g. Goody and Walker, 1972; Manabe and Strickler 1964]. In this state, the net radiative flux at the top of the atmosphere is zero and thus  $R_{net,atm} = R_{net,sfc}$ , where  $R_{net,sfc}$  is the net radiative flux at the surface (positive downward). Thus in a state of radiative convective equilibrium, the atmospheric energy balance as expressed by (2.3a) is equivalent to the surface energy balance

$$\Delta R_{net,sfc} = S + LP. \quad (2.3b)$$

The relationship between changes to atmospheric radiative cooling, namely  $\Delta R_{net,atm}$  (and therefore changes to the surface radiation balance) and changes to precipitation  $\Delta P$  then follows as [e.g. Stephens, 2005]

$$\Delta R_{net,atm} = L\Delta P + \Delta S \quad (2.4)$$

where positive values of  $\Delta R_{net,atm}$  correspond to increased emission of infrared radiation from the atmosphere (i.e. more radiative cooling),  $\Delta S$  is the change in sensible heating and  $L\Delta P$  is the corresponding change in latent heating of the atmosphere determined by a change in precipitation of amount  $\Delta P$ . Figure 2.7 illustrates the energy balance of the perturbed state and shows the changes to the global- and annual-mean atmospheric net radiation ( $\Delta R_{net,atm}$ ) of individual models versus the respective changes in latent heating ( $L\Delta P$ ). This figure indicates that the changes in sensible heating, on the whole, are smaller than the other two components and generally negative. This decrease in sensible heating is the result of the increased infrared opacity of the atmosphere associated with increased water vapor levels in the atmosphere which, in a general state of radiative

equilibrium, acts to reduce the air-sea temperature difference at the surface [e.g. Goody, 1964] thereby inhibiting the sensible heat flux.

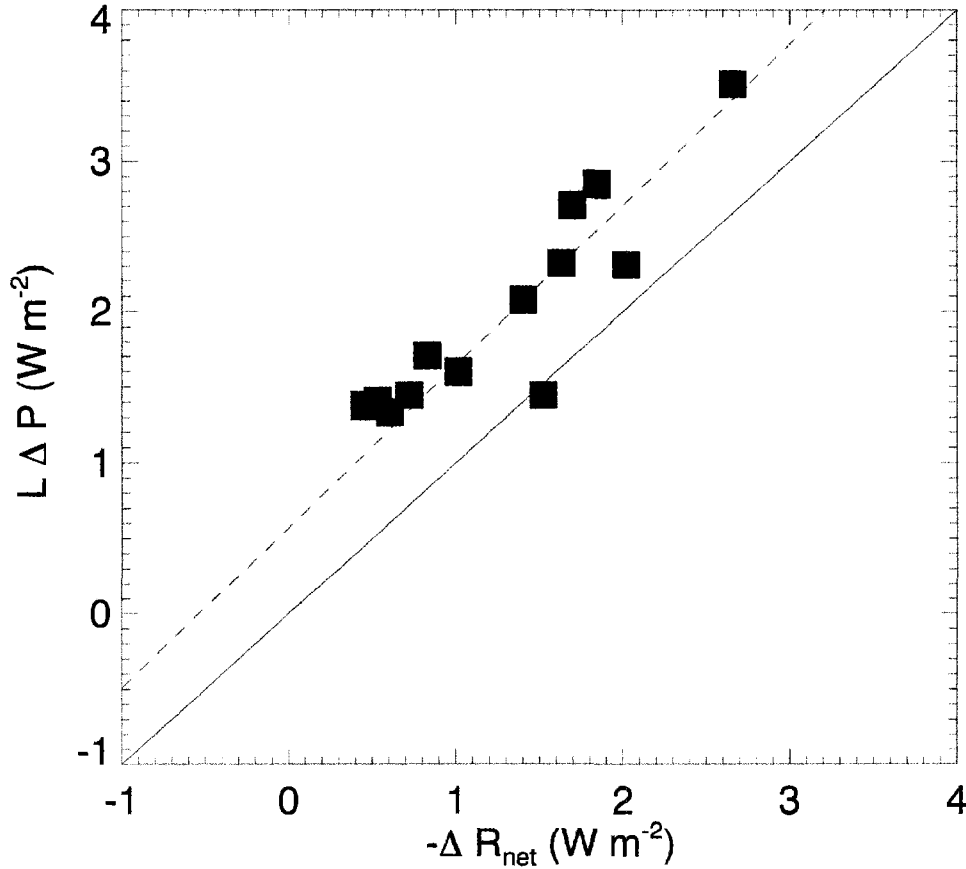


Figure 2.7: The relationship between changes in latent heating ( $L \Delta P$ ) versus changes in atmospheric column cooling ( $\Delta R_{net}$ ) for the AR4 models. The dotted line represents the linear relationship between the two quantities, and the offset between that line and the solid line representing a one-to-one correspondence reflects the contribution of sensible heating to the energy balance.

The loss of radiant energy from the atmosphere  $R_{net,atm}$  can also be conveniently separated into two components [e.g. Stephens, 2005], one due to the clear-sky contribution to this net emission ( $R_{net,clr}$ ) and a second due to changes associated with the absorption and emission by clouds  $C_{net}$  as presented in Figure 2.6. Thus one writes

$$R_{net,atm} = R_{net,clr} - C_{net} \quad (2.5)$$

where a positive value of  $C_{net}$  corresponds to a heating of the column and thus a reduction of the radiative loss of the column. The clear sky term, of order  $100 \text{ Wm}^{-2}$ , is the dominant contribution and its change can be directly related to  $W$  [e.g. Stephens et al., 1994]. The cloud term  $C_{net}$  is much less certain and cannot simply be predicted by water vapor changes. Recent global estimates of this quantity using new satellite observations indicates it is less than  $10 \text{ Wm}^{-2}$  [Stephens et al., 2008]. To first order,  $R_{net,clr}$  varies proportionally with  $W$  according to a power law that owes its existence to the properties of the bulk absorption (and emission) of radiation by strongly absorbing gases like water vapor. The relation between absorption and absorption path is referred to as the curve of growth. A crude but adequate approximation of this curve of growth relation between water vapor and  $R_{net,clr}$  is

$$R_{net,clr} \approx c_0 + aW^b \quad (2.6)$$

where  $c_0$  is the column cooling by all other greenhouse gases in the absence of water vapor and  $b = 0.5$  under the 'square-root law' approximation [e.g. Goody and Yung, 1995]. Values of  $a$ ,  $b$ , and  $c_0$  are derived from a fit to this model obtained for all climate models with sufficient data and for which the fit converged to a single, physically reasonable solution. These parameters, along with the calculated standard deviations in those parameter fits, are provided in Table 2.2 for each successful model fit.

Model	$a$ ( $\text{kg}^{\frac{1}{2}}\text{m}^{2b}\text{s}^{-3}$ )	$\sigma_a$ ( $\text{kg}^{\frac{1}{2}}\text{m}^{2b}\text{s}^{-3}$ )	$b$	$\sigma_b$	$c_o$ ( $\text{Wm}^{-2}$ )	$\sigma_{c_o}$ ( $\text{Wm}^{-2}$ )
CCCMA CGCM3.1	7.61	$3.59\text{e}^{-3}$	0.539	$1.10\text{e}^{-4}$	69.8	$5.23\text{e}^{-3}$
GFDL CM2.0	7.24	$3.66\text{e}^{-3}$	0.536	$1.15\text{e}^{-4}$	69.1	$5.35\text{e}^{-3}$
GFDL CM2.1	17.0	$7.37\text{e}^{-3}$	0.364	$9.16\text{e}^{-5}$	56.0	$8.64\text{e}^{-3}$
INMCM 3.0	5.59	$2.72\text{e}^{-3}$	0.630	$1.16\text{e}^{-4}$	60.4	$4.73\text{e}^{-3}$
IPSL CM4	16.41	$6.23\text{e}^{-3}$	0.408	$7.93\text{e}^{-5}$	53.7	$7.85\text{e}^{-3}$
MIROC HiRes	7.74	$4.12\text{e}^{-3}$	0.510	$1.20\text{e}^{-4}$	73.9	$5.90\text{e}^{-3}$
MIROC MedRes	4.45	$1.26\text{e}^{-3}$	0.623	$6.02\text{e}^{-5}$	75.5	$2.58\text{e}^{-3}$

Table 2.2: Retrieved parameters of the curve fit to the clear-sky atmospheric emission vs. column water vapor curves. Sigma represents the standard deviation in the parameters as returned from the curve fitting routine. Models not appearing on this list either had insufficient data for calculation or the curve fit did not converge to a physically reasonable value.

Using these parameters, three separate approximations illustrate the behavior of  $\epsilon$  as a function of the changes to different energy balance terms in (2.4) and (2.5). Consider first the idealized state of balance governed purely by clear-sky emission and absorption and latent heating:

$$R_{net,clr} \approx LP \quad (2.7a)$$

and thus

$$\Delta R_{net,clr} \approx L\Delta P \quad (2.7b)$$

where one explicitly ignores the contributions changes by  $\Delta C_{net}$  and  $\Delta S$  for the time being. Starting with (2.6) one can first take the derivative of the natural log of both sides, and then by approximating the derivatives by finite differences, obtain

$$\frac{\Delta R_{net,clr}}{R_{net,clr}} \approx \frac{1}{c_o + aW^b} [abW^{b-1}] \Delta W \quad (2.8a)$$

Substituting (2.6) in the left hand side, and bringing  $b$  outside the brackets gives

$$\frac{\Delta R_{net,clr}}{R_{net,clr}} \approx b\Delta W \left[ \frac{aW^{b-1}}{R_{net,clr}} \right], \quad (2.8b)$$

and with rearrangement, one can obtain

$$\frac{\Delta R_{net,clr}}{R_{net,clr}} \approx \frac{b\Delta W}{W} \left[ 1 - \frac{c_o}{R_{net,clr}} \right] \quad (2.8c)$$

Combining (2.8c) with (2.7) and (2.2), one obtains

$$\epsilon_{wv} = b \left[ 1 - \frac{c_o}{R_{net,clr}} \right] \quad (2.9)$$

which will be referred to as the water vapor emission limit on the efficiency. In this case, the ratio of precipitation sensitivity to water vapor sensitivity is determined by the exponent of the curve of growth relationship (2.6) and the normalized magnitude of the growth of emission itself defined from the difference between the atmospheric emission devoid of water vapor ( $c_o$ ) and the atmospheric emission containing the present day amounts of water vapor ( $R_{net,clr}$ ). The reference limit defined in this way is shown in Figure 2.8, including errors bars to denote the range of values possible given the uncertainty of the fits to the data. This figure illustrates that reference limit closely approximates to the actual efficiency derived using (2.2) above. That is to say, the global changes in precipitation of the models analyzed closely follow the change in emission as governed by water vapor changes alone.

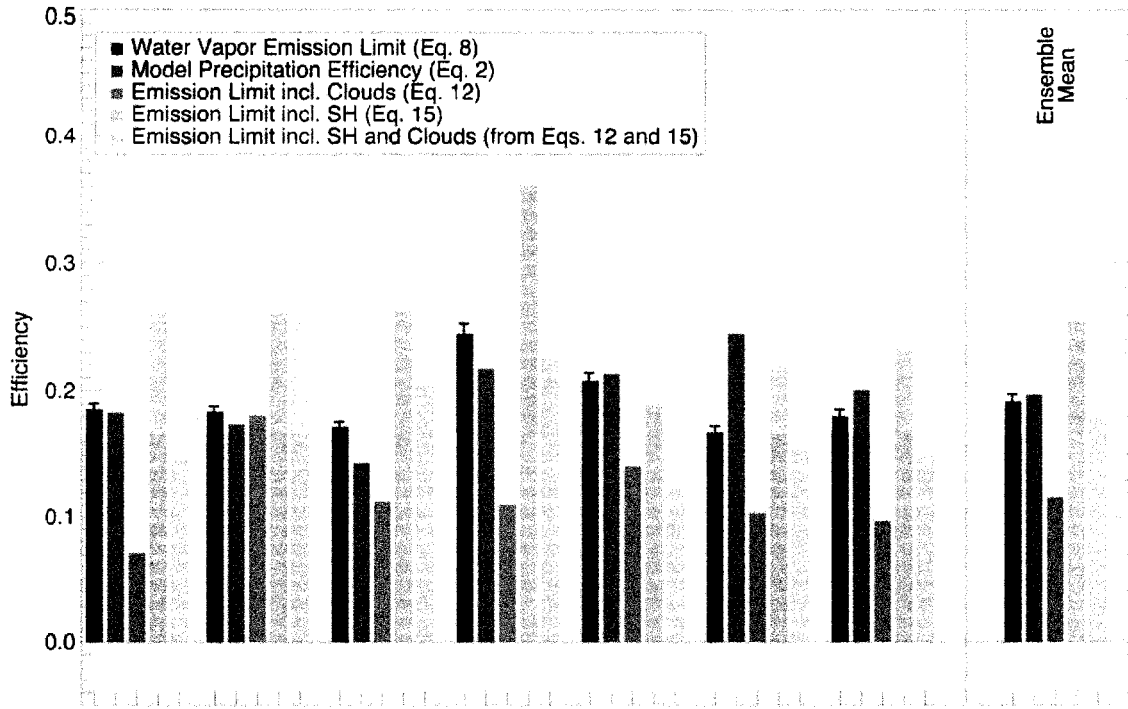


Figure 2.8: A comparison of the model predicted precipitation efficiency  $\epsilon$  to estimates of the emission limit derived from changes in the radiative balance of model atmospheres for selected models. From left to right, the bars represent the water vapor emission limit based solely on changes in clear-sky column cooling for selected models, the predicted precipitation efficiency, the emission limit when including only the radiative effects of clouds, the emission limit when including only the effect of including sensible heating, and the emission limit when including both clouds and sensible heating. The ensemble mean relationships appear in the rightmost set of bars. The error bars on the water vapor emission limit indicate the uncertainty in this limit due to uncertainty from the curve fit parameters  $b$  and  $c_o$  (see Table 2).

Now, consider the contribution of clouds by considering the all-sky energy

balance:

$$R_{net,atm} \approx LP \quad (2.10)$$

and its perturbed form

$$\Delta R_{net,atm} \approx L\Delta P. \quad (2.11)$$

Using equations (2.5) and (2.6), one obtains

$$aW^b \frac{b\Delta W}{W} - \Delta C_{net} \approx L\Delta P$$

and, on rearrangement with some simplification,

$$\epsilon_{\Delta C} \approx b \left[ 1 - \frac{c_o}{R_{net,clr}} \right] - \frac{\Delta C_{net}}{\Delta W} \frac{W}{LP} \quad (2.12)$$

The additional term that appears in (2.12) compared to (2.9) represents the direct effects of cloud feedbacks on precipitation through the contribution of  $\Delta C_{net}$  on the net atmospheric energy balance. Since  $\Delta C_{net}$  is positive (Figure 2.6), then the heating of clouds acts to further reduce the efficiency below the water vapor emission limit. Figure 2.8 illustrates how this contribution is indeed non-negligible and is an important factor in establishing the overall global precipitation efficiency.

The influence of sensible heating on  $\epsilon$  can be deduced in an analogous way by considering the balance

$$R_{net,clr} \approx LP + S \quad (2.13)$$

and its perturbed form

$$\Delta R_{net,clr} \approx L\Delta P + \Delta S \quad (2.14)$$

where cloud effects on the radiance balance are ignored. Following the same steps used to

$$\epsilon_{\Delta S} \approx b \left[ 1 - \frac{c_o}{R_{net,clr}} \right] - \frac{\Delta S}{\Delta W} \frac{W}{LP} \quad (2.15)$$

develop (2.12) one obtains

Since  $\Delta S < 0$  (Fig. 2.9 below), then the second term on the right hand side of (2.15) is positive. Thus reductions in sensible heat flux act to enhance the efficiency  $\epsilon$  illustrated in Fig. 2.8. This is a simple and obvious result that, for a given amount of radiative cooling, any decrease in sensible heating must be offset by an increase in precipitation to provide balance.

## 2.6 Summary and discussion

Figure 2.9 summarizes of the key results and findings of this part of the study by presenting ensemble and global-mean changes in selected model properties. The main conclusions drawn from the study are:

- (i) Column integrated water vapor increases at a rate that resembles a Clausius-Clapeyron (C-C) relationship. Although the majority of water mass increase occurs below 500 hPa (Figure 2.9), the proportional increase of upper tropospheric water vapor is substantially greater than that of the lower atmosphere. Given that upper tropospheric water vapor has a disproportionately large influence on the water vapor feedback [Held and Soden, 2000], the potential influences of the change in upper tropospheric water vapor on the modeled greenhouse effects and the water vapor feedback are topics that warrant further research.

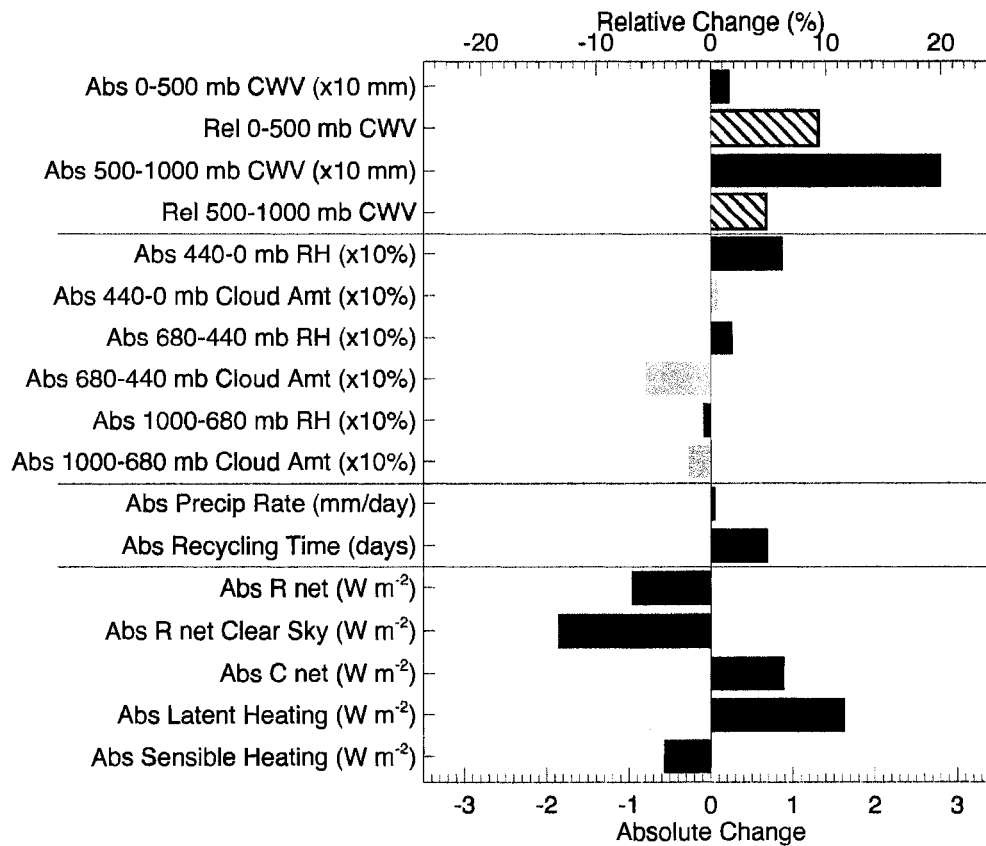


Figure 2.9: A summary of the key findings of this chapter. Absolute (Abs) changes in quantities (filled bars) correspond to the scale at the bottom of the figure and relative percentage (Rel) changes in quantities (hatched bars) refer to the scale at the top.

(ii) Although the water vapor changes in the global model experiments broadly follow the model projected surface warming in a way that resembles a C-C relationship, closer analysis shows that important differences between the model response and the C-C prediction emerge. These differences can be broadly related to changes in the atmospheric circulation of the models and correlate to regional changes in relative humidity and subsequently to precipitation changes. This implies that the regional precipitation changes observed stem from complex changes in circulation and associated relative humidity.

- (iii) Although the absolute global-mean change in lower atmosphere RH is negligibly small (Figure 2.9), the global mean value is comprised of coherent, compensating small regional increases and decreases (Figure 2.2a) that appear to exert a profound influence on the modeled water cycle. It is notable that the regional changes to precipitation correlate significantly to regional changes in lower atmospheric RH (Figure 2.2c and discussion). As noted by others [e.g. Held and Soden, 2006; Seager et al., 2007; Allan and Soden, 2007], the ensemble model results indicate that wet areas gain in precipitation and dry areas are prone to more droughts. The results highlight how small changes in relative humidity, in part induced by shifts in the atmospheric circulation, dramatically influence changes to the model precipitation. The relevance of the association between the circulation and water vapor on precipitation is also noted in Meehl et al., [2005].
- (iv) Global cloud amount decreases in the middle troposphere defined by the layer between 680 and 440 hPa and the slight cloud decreases in the lower troposphere act in a manner to expose the warmer atmosphere below to high clouds thus resulting in a net warming of the atmospheric column by clouds.
- (v) Model predicted water vapor increases per degree of warming occur at a rate that is more than three times the respective rate of increase of precipitation (Figure 2.3). Thus water vapor builds in the atmosphere faster than it can be precipitated out. This result has many implications, two of which are examined. The result clearly points to the influence of factors other than water

vapor alone on global precipitation. As a consequence of these controls, it takes longer for the increasing water vapor in the model atmosphere to cycle through the atmosphere implying a slowing of the atmospheric branch of the hydrological cycle (Figure 2.4b and Figure 2.9). Furthermore, the ratio of global changes in precipitation to global changes in water vapor offer some insight on how readily increased water vapor is converted into precipitation in modelled climate change. This ratio  $\epsilon$  is introduced here as a gross indicator of the global precipitation efficiency under global warming. (Figure 2.4a).

- (vi) Increases in the global precipitation track increases in atmospheric radiative energy loss (Figure 2.7) and the ratio of precipitation sensitivity to water vapor sensitivity is primarily determined by changes to this atmospheric column energy loss. A reference limit to this ratio, namely  $\epsilon_{wv}$ , is introduced and set by the rate at which the emission of radiation from the clear-sky atmosphere increases as water vapor increases. It is shown in Figure 2.8 that the derived efficiency based on the simple ratio of precipitation-to-water vapor sensitivities in fact closely matches the sensitivity derived from simple energy balance arguments involving changes to water vapor emission alone. That is as water vapor increases, the atmosphere cannot emit radiation at a rate that is large enough to require precipitation increases that match the rate of increase in water vapor.
- (vii) Although the rate of increase of clear sky emission is the dominant factor in the change to the energy balance of the atmosphere (Figure 2.9), and in

establishing the efficiency  $\epsilon$ , there are two important and offsetting processes that contribute to  $\epsilon$  in the model simulations studied. One involves a negative feedback through cloud-radiative heating (Figure 2.9) that acts to reduce the efficiency (Figure 2.8). The second is the global reduction in sensible heating (Figure 2.9) that counteracts the effects of the cloud feedback and increases  $\epsilon$ .

Although the global scale influences on precipitation, the main topic of this section, appear to have little direct relevance to the important topic of understanding the character of precipitation change and its regional consequences, these results nevertheless provide a context for developing a broader understanding of this topic. The results explain why the rate at which water is cycled through the atmospheric hydrological cycle must reduce in global warming. There are other indicators that this 'slowing' of the atmospheric branch of the hydrological cycle is occurring in models, such as in the analysis of Held and Soden [2006] who note the reduced convective mass fluxes of models. This slowing of the cycle appears to manifest itself through a combination of less frequent but more intense storm events in models [Tselioudis and Rossow, 2006; Kharin and Zwiers, 2005].

This study also calls out another key point regarding the global control on precipitation changes. When considering global precipitation, the global mean changes in precipitation must be balanced by global mean changes in evaporation from the surface, the only source of water vapor for the atmosphere [Trenberth et al., 2003, Held and Soden, 2006, and others]. One of the important ramifications of this study is that by demonstrating that the increased cooling of the atmospheric column is the primary

constraint on global precipitation, by extension it must also control the global mean evaporation rate. As such, the local changes in moisture transport shown in Figure 2.1c in fact, represent a global mean increase in evaporation at a rate similar to that of the precipitation increase ( $1.3\% \text{ K}^{-1}$ ). This inference is entirely consistent with the general increase in wind speeds noted in that figure, especially over the oceans. However, as Held and Soden [2006] point out in their study of precipitation changes, the response of lower tropospheric moisture is everywhere dominated by the thermodynamically predicted changes in moisture rather than moisture transport. The results of this study confirm those results.

This study raises a number of questions. Are observed changes in global precipitation consistent with a rate of change that mirrors both the observed and modeled changes of water vapor or are they consistent with the notion that the growth of precipitation, controlled by energetics, is constrained for reasons mentioned in this chapter? Strong evidence exists to suggest that the observed water vapor content of the atmosphere is increasing at rates similar to that projected by climate models, at least over oceans [e.g. Trenberth et al., 2005; Santer et al., 2007]. A number of studies suggest that the frequency of intense precipitation (e.g., the frequency of very heavy precipitation or the upper 0.3% of daily precipitation events) has increased over half of the land area of the globe [e.g. Groisman et al., 2005]. The studies of Fu et al. [2006] and Mitchell et al. [1987] also suggest that the areal extent of regions of the subtropics that comes under the influence of broad-scale subsidence might also be expanding in time, broadly consistent with the model drying tendency in the subtropics as implied in Figure 2.2. This result

appears to have been confirmed in the study of Allan and Soden [2007] who find that precipitation is observed to have decreased in descending regimes that typically define dry climatic regions between 30°N and 30°S. Although one might expect that the broad changes in precipitation distribution are shaped by changes to the large scale circulation, Emori and Brown [2005] suggest that the noted precipitation increases by more intense storms in models is governed by thermodynamics rather than changes in atmospheric circulation.

Results of a number of recent studies seem to conflict with the results presented in this study. For example, Gu et al. [2007] analyze 27 years of GPCP data, as do Allen and Soden [2007], and find a trend in the tropical precipitation over oceans more similar to the stated water vapor trend (i.e.  $\epsilon \approx 1$ ) than the projected trends of climate models. Zhang et al. [2007] report on analysis of 75 years of surface rain gauge data and note observed, regional changes of both signs are larger than modeled changes. Wentz et al. [2007] recently reported on a study that merges different global precipitation data sources, including GPCP, with their own microwave-based precipitation estimates, together with inferences on evaporation, and estimate a change in global precipitation of 6% K<sup>-1</sup> which again implies  $\epsilon \rightarrow 1$ .

At first glance, it would appear from these studies that the models significantly underestimate the increase in precipitation suggested from observations. These observationally-based studies seem to suggest that the rate of increase of precipitation ought to be similar to the rate of increase of water vapor, i.e  $\epsilon \approx 1$ , yet the robust, physical constraints described in this paper suggest that  $\epsilon < 1$  is to be expected and, in

fact, much closer to the values predicted by models. Feedbacks could occur in the real climate system that change the nature of the constraints discussed in this paper increasing  $\epsilon$  toward the C-C value, although it is difficult to see how these feedbacks could alter the energy balance enough to push  $\epsilon$  to unity. For example, cloud changes could occur that are the reverse of those shown in Figure 2.5, such as by substantial decreases in high cloud and increases in low cloud thereby adding to the water-vapor induced atmospheric cooling. The analysis of this paper suggests this feedback would have to approximately quadruple the magnitude of the water vapor based cooling perturbation for  $\epsilon \rightarrow 1$  and this seems unrealistic given the net, global radiative heating of the atmosphere by clouds in the present climate is almost an order of magnitude smaller than that due to water vapor [Stephens et al., 2008].

This brings the focus on the observations studies themselves and, in particular, a focus on the observing system uncertainties related to those studies. The observations reported in most of these studies are not global, being restricted to over land [e.g. Zhang et al., 2007], or limited to the tropics [Allan and Soden, 2007] and thus can neither confirm nor refute the results of this paper. The only truly near-global (land and ocean) data source of precipitation is that of GPCP and much care is needed in interpreting any trend in these data as Gu et al. [2007] caution. GPCP data are a heterogeneous mix of satellite data of different types and sensitivities to precipitation (based on infrared and microwave radiances) as well as surface rain-gauge data [Huffman et al., 1997] and real uncertainty in the precision of these data has yet to be established. Gu et al. [2007] note that “the global linear change of precipitation is near zero” (one might estimate less than

1% K<sup>-1</sup> based on their trends) yet Wentz et al. [2007] using their own satellite microwave-based product over oceans combined with the over-land GPCP arrive at a conflicting result with precipitation changes approaching 6% K<sup>-1</sup>. Lambert et al. [2008] suggest that, while the precipitation may be changing at 6% K<sup>-1</sup>, the error on those measurements maybe up to 3% K<sup>-1</sup>. This merely highlights the inconsistencies in the global data sources themselves and, coupled with the difficulties that arise from calculating decadal-scale trends with data that span a relatively short time period, serves as reminder that trends in these data should be treated cautiously at this time.

The following chapter presents a new data source that may help to address some of this uncertainty. The CloudSat satellite [Stephens et al., 2002], which has been in orbit since 2006, provides data that can be used to detect the incidence and intensity of precipitation of the global oceans. It will be shown that this new algorithm, the details of which can be found in brief in the next chapter and in more detail in Haynes et al. [2008], provides more detailed knowledge of where precipitation is occurring and the kinds of cloud structures associated with that precipitation. This data can not only eventually help to understand changes in precipitation, but as will be shown, can be used to evaluate how weather and climate models predict precipitation and the clouds associated with them which, as this chapter has shown, has extremely important implications for the radiative budget of the atmosphere and the prediction of climate change and its consequences.

# **Chapter 3: Precipitation Incidence from CloudSat: Validation and Model Evaluation**

## **3.1 Introduction**

Observing changes in global precipitation is a topic of vital importance to the scientific community. Several recent studies [e.g. Allen and Ingram, 2002; Held and Soden, 2006; Stephens and Ellis, 2008] have argued that there are robust physical reasons why the average precipitation rate will likely increase in response to an increase in carbon dioxide in the atmosphere. Furthermore, Trenberth et al. [2003] argues that the nature of these changes are such that rainfall events are expected to become less frequent while at the same time more intense. Interestingly, it has been shown that while both weather forecasting and climate forecasting models predict changes in global precipitation frequency consistent with theoretical arguments [e.g. Tselioudis and Rossow, 2006; Kharin and Zwiers, 2005], they often do so through an incorrect combination of frequency and intensity [Sun et al., 2006, and references therein]. To increase scientific confidence in such predictions, these models should be able to reproduce both the frequency and intensity of precipitation as observed in the current climate system.

The initial problem, therefore, is that before one can evaluate such models, one must identify an adequate dataset for the model comparison studies. Satellite datasets of precipitation are ideally suited for such comparisons due to their near-global coverage.

However, conventional satellite-based observations of precipitation frequency suffer from a lack of sensitivity to light precipitation either due to instrument limitations or an inability to distinguish between light rain and cloud [Berg et al., 2006]. Petty [1997] found that ten special sensor microwave/imager retrieval algorithms often failed to detect precipitation at high latitudes or in regions of showery trade cumulus precipitation. Given that Haynes and Stephens [2007] showed that trade cumulus precipitation likely occurs more frequently than was once believed, this is a serious shortcoming.

To that end, the new precipitation product [Haynes et al., 2008] from the millimeter-wave spaceborne Cloud Profiling Radar (CPR) [Im et al., 2005], flying in the A-Train constellation on board CloudSat [Stephens et al., 2002] provides a unique opportunity to perform such comparisons over the global oceans. However, before model comparisons can be conducted with new data such as these, the new data must first be vetted through comparison with widely-accepted existing datasets such as the ground based [e.g. Sun et al., 2006; Dai et al., 2001a, and others] and ship-based [e.g. Petty, 1995] data that have been used repeatedly. These data present technical challenges because they are neither global nor homogeneous and are often taken by various observing platforms. Yet, through careful quality control, they provide highly-suitable sources of data that test the detection of precipitation in a variety of locations around the world.

Once the CloudSat precipitation data have been verified using the existing incidence data, the door is open for analyzing the characteristics of precipitation clouds over the oceans from the perspectives of both observation and model. In particular, this

study seeks to examine how often it rains over the global oceans and what kinds of clouds are producing the rain. Furthermore, with special model runs of the state-of-the-art European Center for Medium-Range Weather Forecasting (ECMWF) weather model (more information at <http://www.ecmwf.int>) and the Met Office Unified Model HadGAM1 [Martin et al., 2006], it is possible to examine the types of clouds that produce precipitation in various regions around the world in these models in the hopes of gaining new insights into how precipitation is produced in models as well as in the observable atmosphere.

## **3.2 Data and Methodology**

### **3.2.1 The CloudSat Precipitation Algorithm**

In addition to its well-documented ability to profile clouds in the atmosphere [e.g. Mace et al. 2007, Posselt et al. 2008], the combination of path-integrated attenuation (PIA) and high sensitivity radar reflectivity observations from CloudSat's 94 GHz (W-band) nadir-pointing CPR provide an ideal combination of measurements for detecting precipitation with a high degree of confidence. Haynes et al., [2008], for example, outline an approach that uses surface wind speed, sea surface temperature, and atmospheric temperature and moisture profiles over the oceans from the ECMWF weather model to determine the theoretical backscatter cross section of the surface in the absence of hydrometeors. Comparison of the radar-observed backscatter cross section against this theoretical model provides a means of measuring the PIA, which in turn can be used to detect the presence, and often the intensity, of precipitation.

Following Haynes et al., [2008] the sum of the observed near-surface radar reflectivity (480 m and 720 m above sea level) and the contributions from PIA and gaseous attenuation provides an estimate of the unattenuated near-surface reflectivity value. The larger the value, the more likely that precipitation is occurring. Thus, threshold values of this reflectivity can be chosen to indicate the likelihood of precipitation. For rain, the threshold reflectivity over which precipitation is certainly occurring is approximately 0 dB [Schumacher and Houze, 2000]; reflectivities between -15 dB and 0 dB indicate that drizzle is probably occurring [Frisch et al, 1995, Stevens et al, 2003]. For snow (i.e. when the entire atmospheric temperature profile is below 0°C), the threshold for certain precipitation is approximately -5 dB. The result is an algorithm that, unlike other spaceborne precipitation radars, is sufficiently sensitive to the presence of small water droplets that even incipient precipitation can be detected [Stephens and Haynes, 2007]. Furthermore, unlike passive microwave sensors that suffer from an inability to distinguish cloud and precipitating liquid, the use of reflectivity ensures that sufficient numbers of large droplets exist to guarantee the presence of precipitation. In heavy rain events when the CPR signal may be fully attenuated, this algorithm will still mark the presence of precipitation, allowing the detection of precipitation events across a full spectrum of intensities. Finally, the use of low-level reflectivity data make it likely that detected precipitation is actually reaching the ground.

To evaluate this product, it is compared with two existing surface data sets that provide precipitation occurrence data over the oceans, albeit with much less spatial coverage: the International Comprehensive Ocean-Atmosphere Data Set (ICOADS) 2.4

ship-based data [Worley et al., 2005], and Global Summary of the Day (GSOD) precipitation data [Lott and Baldwin, 2002] available from the National Climatic Data Center (NCDC). The following sections include information on each of these datasets and how they are used.

### **3.2.2 The International Comprehensive Ocean-Atmosphere Data Set (ICOADS)**

The ICOADS dataset includes a wealth of standard ship synoptic weather data as well as a series of valuable quality control flags that can be used to parse those data. This portion of the study constructs a global-ocean climatology of precipitation incidence using primarily the present weather observation (IMMA code “ww”) reports extracted from the ICOADS dataset for the time period covering August 2006 – July 2007 in order to overlap the first full seasonal cycle captured by CloudSat.

This study closely approximates the methods of Dai [2001a] and Petty [1995], including the extensive quality control measures used to avoid various errors often found in ICOADS data. For an observation to be considered valid, the algorithm implemented in this study requires it to pass a series of three checks. First, the internal quality control (QC) flags for seas surface temperature (SST) must be valid. As such, the algorithm requires that the NCDC-QC flag (IMMA code “SNC”) equals 1 (which indicates a correct, internally consistent value of SST) and/or the adaptive ICOADS QC flag (IMMA code “SQZ”) is between “D” and “N” (which indicates that the data are within 2.5 standard deviations of the smoothed climatological SST for that region). As in Petty [1995], the intent of this procedure is to reduce the impact of mislocated reports, especially in the southern oceans where there is already a dearth of observations.

Secondly, the algorithm checks the station/weather indicator flag (IMMA flag “IX”) to see whether or not the a missing weather report is due to a lack of observable weather or a missing report altogether; for this study, “IX” flag values of 1, 2, 4, or 5 are considered valid observations. Finally, the algorithm checks to make sure that there is a non-missing cloud observation (IMMA code “N”). In Petty [1995], this check was implemented to avoid errors due to missing weather codes reported due to a lack of reportable phenomena. While at first glance, this might seem to be redundant with the check of the “IX” flag, Dai [2001a] reported inhomogeneities that were attributed to the introduction of the “IX” flag in 1982 and its inconsistent use. In light of this report, this study applies both quality checks to keep reporting errors to a minimum.

The main difference between this study and those of Petty [1995] and Dai [2001a] is found in the selection of a different subset of the present weather codes as precipitation events. Table 3.1 lists the code numbers used in this study, which were selected to include both rain and snow so to represent both “possible” and “certain” precipitation events that CloudSat might be able to detect. Any code not listed in Table 3.1 is classified as non-precipitating. While “certain” events are those that would definitely be detected by the CPR, “possible” events include a variety of reports including: precipitation reported within sight of, but not at the ship, events related to precipitation (such as lightning) but without an actual precipitation report, precipitation in the hour preceding the observation, potentially small-scale events such as thunderstorms and showers, and freezing rain. Due to extraordinary amount of detail included in each of the weather codes, the reader is referred to the extensive listing in Dai [2001a, Table 1] for

more details on these classifications rather than duplicating them here. More importantly, the difference between the number of observations that include only “certain” precipitation events and the number of observations that include both “possible” and “certain” precipitation provides a range of acceptable values of frequency of precipitation incidence for comparison to the satellite observations. Finally, due to the spatial inhomogeneity of ship-based reports, both the ICOADS reports and CloudSat data are zonally averaged into 2.5 degree latitude bands. This also provides the advantages of increasing the number of observations used in the calculations and giving a more global sense of the agreement between CloudSat and the ship-based observations.

Certain	Possible
50,51,52,53,54,55,	13,14,15,16,17,18,
58,59,60,61,62,63,	19,20,21,23,24,25,
64,65,80,81,82,91,92	26,27,29,56,57,66,
	67,68,69,83,84,87,
	88,89,90,93,94,95,
	96,97,98,99

Table 3.1: WMO present weather codes (“ww”) used to classify ICOADS precipitation events as possibly or certainly detectable by CloudSat. See Dai [2001a] for more details on these codes.

**3.2.3 Global Summary of the Day (GSOD) Station Data**

One drawback of performing analyses using only zonal averages is that they eliminate the opportunity to evaluate precipitation occurrence statistics for individual locations and/or individual systems. To address this concern, this study also compares

daily precipitation reports extracted from the GSOD dataset for a collection of island stations, sea platforms, and moored buoys from around the globe. These data, which span the years 1929 through present, report eighteen surface meteorological elements for each day (0000 – 2359 UTC) and present both daily ranges and averages calculated from synoptic and hourly data sources. The ingested data are run through extensive automated quality control before they may be considered valid and at least four separate valid observations are required to create one valid summary of the day.

For this study, GSOD data from August 2006 – July 2007 are used to coincide with the other two datasets. This was accomplished through a painstaking process that combined both objective and limited subjective selection criteria. First of all, all locations were examined by hand to ensure that they were in fact islands and not part of a continental landmass. Secondly, all data sites with elevations over 100 meters were discarded in order to select sites that would be more ocean like and less affected by orography. Finally, stations located on large islands (usually islands with multiple reporting stations) and stations located on islands within close proximity of continental land masses were also eliminated. This left 544 stations in 2006 and 885 in 2007 with data available for comparison to CloudSat. This mismatch in the number of stations available for each year, however, is not an issue due to the nature of the calculation of the precipitation incidence for this product. Since GSOD data provide total daily precipitation, these data can only be used to calculate the frequency of “rain days,” which is defined for GSOD as a day when non-zero liquid equivalent precipitation or a trace of precipitation (precipitation flag “H”) was reported. Therefore, the precipitation incidence

for a station is simply the proportion of “rain days” to the total number of days for which valid observations are available.

One must also note the difficulty in comparing a surface observation at a point to a satellite observation that may not pass directly overhead. This study includes any CloudSat observations that pass within the 2.5 x 2.5 degree box centered on the station’s location on a given day. This certainly inflates the number of “rain days” CloudSat would detect when there is non-zero rain rate in the box around a station. However, that inflation must be weighed against the difficulty of using a smaller bounding box results in too few observations to obtain a reliable estimate of precipitation incidence. In this case, the reliability of the statistics from CloudSat outweighed the desire to use a smaller grid size, though it is hoped that with a longer span of data one would not have to choose.

### **3.2.4 The European Center for Medium-Range Weather Forecasting (ECMWF)**

#### **Weather Forecast Model**

For the purposes of comparison with CloudSat, two sets of model prediction experiments were performed to include specific information on the vertical structure of clouds associated with model-predicted precipitation. One set of model data were provided by Angela Benedetti of ECMWF using a special run of the Integrated Forecasting System (IFS) for the time period June–August 2007. This was a standard forecast configuration of model release cy31r2 with 60 vertical model levels and a horizontal resolution of T511 [Benedetti, personal communication]. The only significant difference from a standard run is that the model saved non-standard output on precipitation for cloud top heights below 4.75 km, between 4.75 km and 11 km, and

above 11 km following the analysis of Haynes and Stephens [2007]. For more information on all of the physical schemes implemented in this model, the reader is referred to the most recent information available in the online documentation at <http://www.ecmwf.int> and the technical memo on the model physics by Tompkins et al. [2004].

Precipitation often falls from layered cloud systems, with lower precipitating clouds existing under a canopy of higher clouds such as anvil cirrus from distant cumulonimbus [e.g. Stephens and Wood, 2007]. Therefore, when layered clouds are precipitating, it is important to distinguish between the precipitating clouds and the non-precipitating clouds above them. Therefore, the cloud top height data were calculated in two different ways in an attempt to identify these different clouds. The first method counts up from the bottom of the model until the top-most layer where the precipitation rate was found to be greater than  $0.05 \text{ mm hr}^{-1}$  was located. This method has the advantage of most closely identifying the top of the precipitating cloud in cases where there are multiple cloud layers. The other method locates cloud top height by examining model layers from the bottom up and looking for the top-most layer where the model drops below threshold values of cloud (1%), liquid water content ( $0.02 \text{ g m}^{-3}$ ), and ice water content ( $1.7 \times 10^{-3} \text{ g m}^{-3}$ ). This method provides cloud top heights similar to “traditional” cloud-top heights most commonly observed by passive microwave or visible satellite imagery. It should also be noted that using a rain rate of  $0.05 \text{ mm hr}^{-1}$  is not common practice; most observations use a threshold of  $0.01 \text{ mm hr}^{-1}$ . However, in this case the higher threshold is closer to where the lower detection threshold of CloudSat lies

[Haynes et al., 2008]. While not shown, this choice of thresholds has no significant bearing on the results.

### **3.2.5 The HadGAM1 Climate Configuration of the Met Office Unified Model**

The other model data source is provided by Alejandro Bodas-Salcedo using simulations from the atmosphere-only version of the latest climate configuration of the Met Office Unified Model (MetUM), referred to as HadGAM1. HadGAM1 uses a horizontal resolution of 1.25 degrees latitude by 1.875 degrees longitude, and has 38 vertical levels, the top level being at around 39 km. The dynamical core is a two-time level semi-implicit, semi-Lagrangian formulation and is also non-hydrostatic [Davies et al., 2005]. A more detailed description of HadGAM1 and its physical packages is given in Martin et al. [2006]. Its performance in terms of global climatology, variability, regional climate, and surface radiation budget can be consulted in Martin et al. [2006], Ringer et al. [2006], and Bodas-Salcedo et al., [2008].

The model is forced with present-day (1980 to 2000) observed climatological sea surface temperatures (SSTs), and run for 15 years. Three-hourly cloud and precipitation fields are extracted for the last five JJA seasons and the maximum and minimum cloud tops for those grid boxes where precipitation occur are output for analysis. These are again broken down by height into the same cloud height bins following the work of Haynes and Stephens [2007]. Furthermore, the maxima and minima again provide an opportunity to evaluate precipitation from layered cloud structures. The minimum cloud top height data can be used as a way of representing the height of the precipitating cloud in a layered system, while the maximum cloud top height can be used for comparison to

the “traditional” cloud top height as before. For the sake of comparison, the same precipitation threshold of  $0.05 \text{ mm hr}^{-1}$  is applied to these data as well. There is one additional point worth noting, however. At this time, the HadGAM1 model cannot output vertical cloud profiles for convective precipitation, which means that in those cases the minimum and maximum cloud top heights are identical. It is believed that this is not an issue since model convective cloud is rarely multilayered [A. Bodas-Salcedo, personal communication].

### **3.3 Results and Discussion**

#### **3.3.1 Surface-based validation**

Figure 3.1 presents zonal-mean comparisons of the CloudSat frequency of precipitation occurrence, including certain rain events (asterisks) and certain rain and certain snow events (filled circles) to the ICOADS ship-based reports (grey bars) in the annual mean (Figure 3.1a), as well as in each of the four seasons (Figures 3.1 b–e). The meridional patterns of precipitation exhibited in these plots are consistent with the results of Petty [1995] using ship-based data alone. The ITCZ is evident in all plots and precipitation increases in the winter hemispheres due to mid-latitude storms. In the annual mean (Figure 3.1a), the frequency of occurrence of rain and snow detected by CloudSat falls within the range of values one would expect based on the ICOADS data between the latitudes of  $60^{\circ}\text{S}$  and  $70^{\circ}\text{N}$ . This is a very encouraging result, illustrating how well the sensitivity of the CPR performs at detecting snowfall in the high latitudes. The seasonal cycle of precipitation frequency as detected by CloudSat (Figures 3.1 b–e) is also consistent with that observed from the ICOADS data, showing the precession of

precipitation maxima to the winter hemisphere as well as the slight migration of the rainfall maximum associated with the poleward migration of the ITCZ over the Pacific Ocean in boreal summer and fall.

There are some caveats worth noting as well. First of all, it is impossible to evaluate the performance of CloudSat poleward of 60°S or 70°N due to a lack of ship-based data. In these regions, there are fewer than 10 ship-based observations for the entire year. Therefore, while the excellent agreement at all other latitudes suggests that these data are reliable as well, CloudSat observations poleward of these latitudes should be treated with additional caution. Additionally, one might note that CloudSat observations are always at the low end of the ICOADS range of precipitation incidence observations, and in some cases (particularly in the tropics) the CloudSat data appear to indicate fewer instances of precipitation than ICOADS. This is likely due to the fact that only observations flagged as certain precipitation were included in this analysis. Were CloudSat observations that had been flagged as probable rain or snow events also included in this analysis, CloudSat incidence values would all fall well within the ICOADS ranges. For this presentation, however, it was deemed more instructive to show that, even using the most strict thresholds, the performance of the CloudSat retrieval was consistent with the ship-based data.

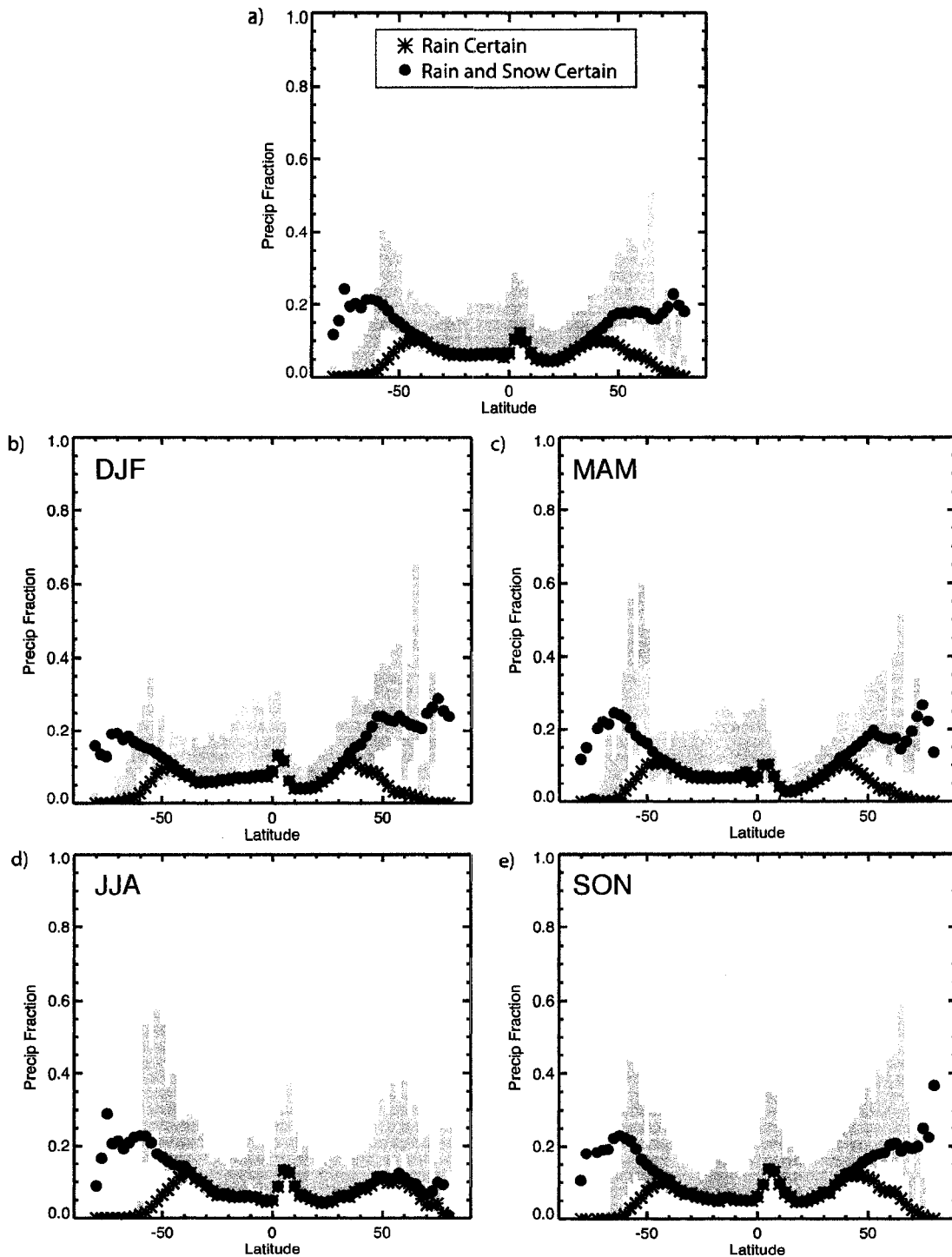


Figure 3.1: (a) Zonal mean annual mean precipitation incidence as reported by CloudSat for August 2006–July 2007 including only rain reports (circles) and both rain and snow reports (stars) compared against a range of values that represent the range of possible precipitation incidence values for that latitude band based on ICOADS ship reports for the same period, (b) The same but for DJF only, (c) MAM only, (d) JJA only, (e) SON only.

Figure 3.2 shows how CloudSat data compare to the selected GSOD stations for the period from August 2006 – July 2007. Figure 3.2a presents the annual mean, while Figures 3.2b–e show the comparisons for each of the four seasons. Overall, the number of rain days as determined from CloudSat compares favorably to those determined from the station data from GSOD. The scatter about the one-to-one ratio line (solid diagonal line) appears qualitatively to be quite good considering that it is a comparison of satellite observations in 2.5 x 2.5 degree boxes to point observations. There doesn't appear to be a seasonal dependence to the relative performance of CloudSat to GSOD.

There are a significant number of reports where CloudSat reported rain days around stations where no rain days were reported. In many cases, this is likely due to the larger observing area afforded to the definition of a rain day for CloudSat. It is simply more likely that it will rain in an area several hundred square kilometers in size in a given day. However, in some cases this may also be due to poor quality or few valid reports in the GSOD data. And in some cases, it may be the climate of particular stations that place them in rain shadows that are otherwise undetectable without a much more thorough analysis. These anomalous data points are illustrative of the difficulties inherent in performing validation studies. Nevertheless, the large number of data points that do not appear to exhibit any of these issues seems to indicate that there seems to be little significant impact on the study.

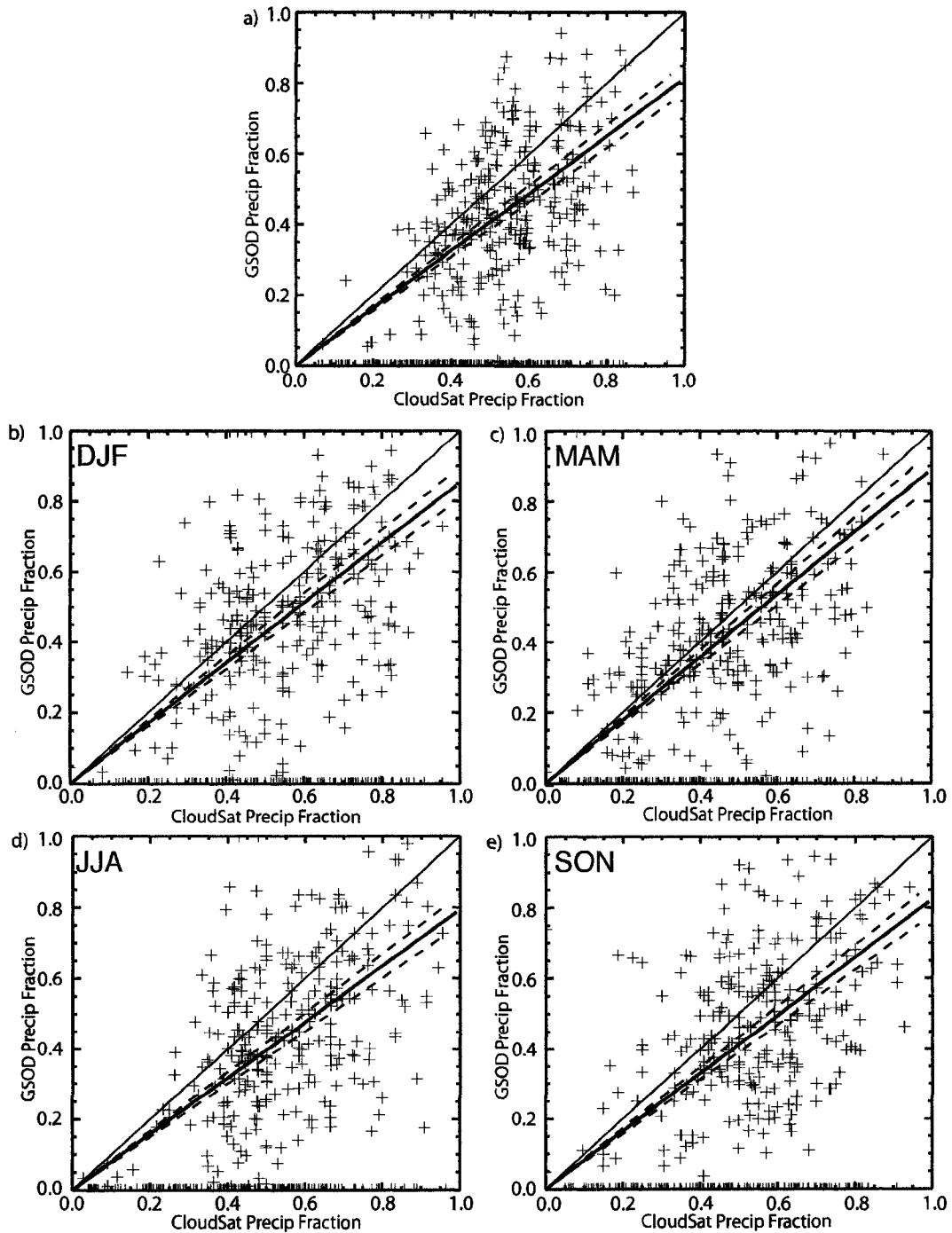


Figure 3.2: (a) Annual mean scatter plot of GSOD precipitation incidence (precip fraction) to the CloudSat precipitation incidence in the  $2.5 \times 2.5$  degree boxes surrounding those stations. The thin solid line represents a slope of one, and the thick solid line flanked by dotted lines represents the best fit through zero for the data. The slope of this fit is  $0.80 \pm 0.04$ , (b) The same as (a), but for the DJF season, with a fit of  $0.78 \pm 0.04$ , (c) MAM, fit is  $0.81 \pm 0.04$ , (d) JJA, fit is  $0.84 \pm 0.05$ , (e) SON, fit is  $0.87 \pm 0.05$ .

In addition to the raw scattered data, each figure shows the least-squares linear fit to the data (excluding the anomalous data discussed previously), bounded by the 95% confidence intervals in the slope parameter. The slope of the fit to the annual mean is  $0.80 \pm 0.04$  and ranges from 0.78 in JJA to 0.87 in MAM. The correlation coefficients for each fit were between 0.83 and 0.85. These fits indicate that there is a slight bias towards higher precipitation incidence as observed by CloudSat. As mentioned in the previous section, a bias toward CloudSat would be expected because, by including a larger possible area for precipitation to occur, the probability of precipitation occurring necessarily would increase. It may be possible in the future to mitigate this effect by requiring that a threshold number of consecutive rainy pixels be detected before the CloudSat rain day flag be set, since this would potentially limit rain days to large-scale organized precipitation that likely would affect the station as well.

Despite the uncertainties inherent in using ground based data to validate the precipitation incidence observed by CloudSat, there are plausible explanations for nearly all of the anomalous incongruities between the datasets. Furthermore, those uncertainties are diminished in the face of the otherwise excellent agreement, especially with the measurement of snow in high latitudes and the precession of precipitation maxima with seasons. Thus, one can conclude from this analysis that CloudSat reliably retrieves the incidence of precipitation from space and should be used to further understand the nature of precipitation processes in the climate system.

### 3.3.2 CloudSat Precipitation Incidence

Figure 3.3 presents the frequency of precipitation incidence as observed by CloudSat for the period August 2006–July 2007. Figure 3.3a provides a 2.5 x 2.5 degree map of the annual mean of the precipitation incidence (including scenes classified as certain rain and certain snow). Notable features include the relatively high frequencies of precipitation occurrence (greater than 20%) in the inter-tropical convergence zone (ITCZ) and the mid-latitude storm tracks roughly poleward of 40 degrees latitude. Though not shown by this figure, it can be deduced in combination with Figure 3.1 that much of the precipitation observed by CloudSat poleward of 50 degrees latitude is falling as snow. The global mean precipitation incidence derived from this map (rain and snow) is 11.2%; the global mean including only rain is 9.0%. As a basis of comparison, the precipitation incidence calculated from the AMSR-E instrument [Wilheit et al., 2003] flying aboard Aqua in the A-Train constellation is only 4.3%, showing the drastic underdetection of precipitation by the passive microwave sensor. Figure 3.3b shows the zonal-mean seasonal cycle of the same data. There are several important features of the seasonal cycle of CloudSat observations worth calling out. First of all, one should note that CloudSat data appear to reflect the reduced precipitation in the midlatitudes of both hemispheres during their respective summers due to reduced numbers of mid-latitude baroclinic storms in the summer months. The northward shift of the tropical precipitation in the boreal summer and fall suggest the detection of the northward migration of the ITCZ during those seasons. Finally, CloudSat data suggest that the seasonal cycle of precipitation incidence has a larger amplitude in the northern hemisphere. This is likely a

signal of the larger reservoir of available potential energy for mid-latitude storms due to the larger temperature gradients created by the greater land mass in the north. All of these features are consistent with the results of Dai [2001a]. These observations, particularly those regarding precipitation in the poleward of the tropics, showcase the utility of the observations that CloudSat is uniquely situated to provide.

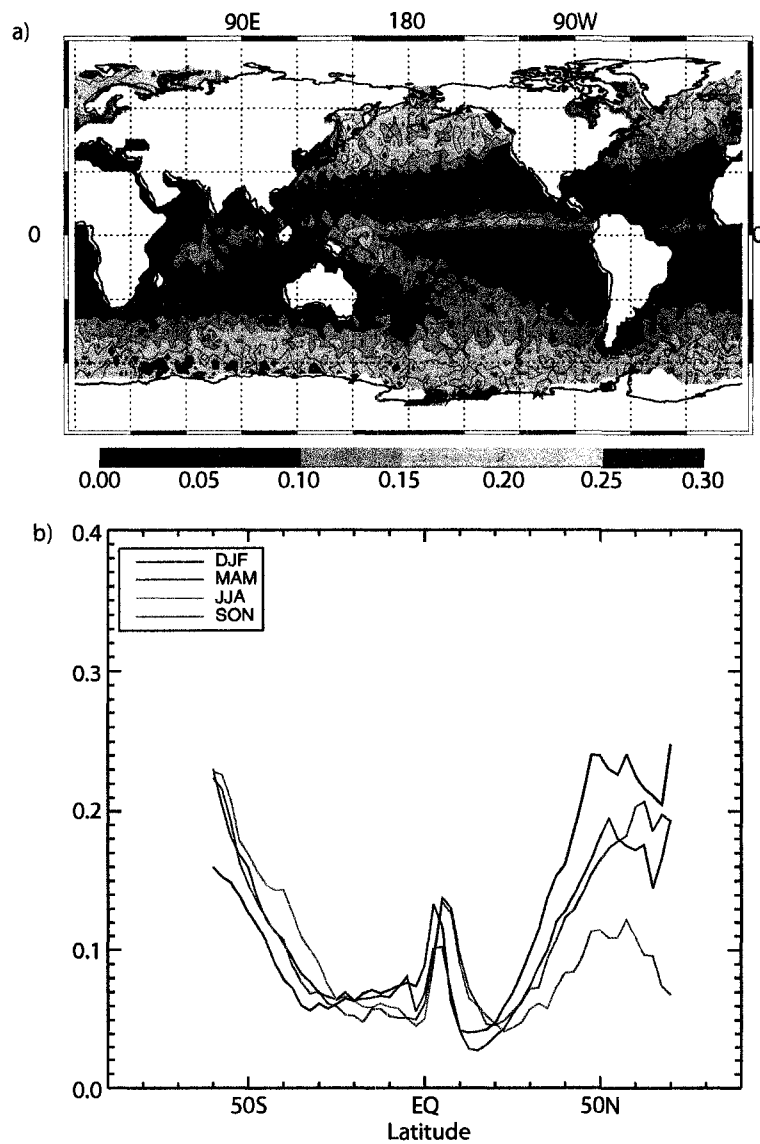


Figure 3.3: (a) Annual mean frequency of precipitation incidence as observed by CloudSat for the period of August 2006–July 2007. (b) Zonal mean frequency of precipitation incidence as observed by CloudSat for each individual season, illustrating the observed seasonal cycle of precipitation incidence.

Now looking specifically at June-August of 2007 (for comparison to the models shown subsequently), global maps of the types of clouds detected when CloudSat detects rain or snow are shown in Figures 3.4 and 3.5. Figure 3.4 presents the relative frequency of occurrence of lowest cloud top height (CTL) when precipitation is detected, while Figure 3.5 presents the relative frequency of occurrence of the highest observed cloud top height (CTH). In each case, the cloud heights are broken down into the three height bins defined in section 3.2.4: low clouds below 4.75 km, mid-level clouds between 4.75 and 11 km, and high clouds above 11 km. Again, it is important to keep in mind that CTL best represents the cloud top height of the precipitating cloud in a layered cloud structure while CTH often represents the cloud traditionally referred to as “cloud top height” and which is most often observed by passive microwave satellite sensors.

The results of Figure 3.4 show many interesting features. In the tropical oceans, precipitation predominantly falls from low level clouds (Figure 3.4a), particularly in the regions most noted for the presence of marine stratocumulus cloud and trade cumulus cloud. Poleward of those regions, precipitation appears to be relatively equally partitioned between all three cloud types, although it appears that high cloud tops, which likely signal the frequent occurrence of deep convection, rarely occur poleward of 45 degrees latitude and when they do occur, they appear to be located in regions that would be associated with frontal passage (Fig 3.4c). In the tropical west Pacific ocean, precipitation appears to fall equally from both deep convective and mid-level clouds, but there is a dearth of low-level precipitating cloud in this region. The mid-level mode (Fig 3.4b) accounts for 20-60% of the precipitation near the ITCZ and the South Pacific

Convergence Zone (SPCZ) and further suggests the importance of shallow convection (i.e. the congestus mode [Johnson et al. 1999]). Finally, one can also infer vertical heating profiles from the depth of the precipitating clouds, where deeper precipitating clouds would have higher latent heating peaks from the formation of precipitation. In general, these results appear to confirm the previous findings of Schumacher et al., [2004], who used the Tropical Rainfall Measurement Mission (TRMM) Precipitation Radar to calculate vertical latent heating profiles in the tropics and found that the peak heating was generally lower in the eastern Pacific (around 700 hPa or ~3 km) and higher in the western Pacific (around 400 hPa or ~7 km).

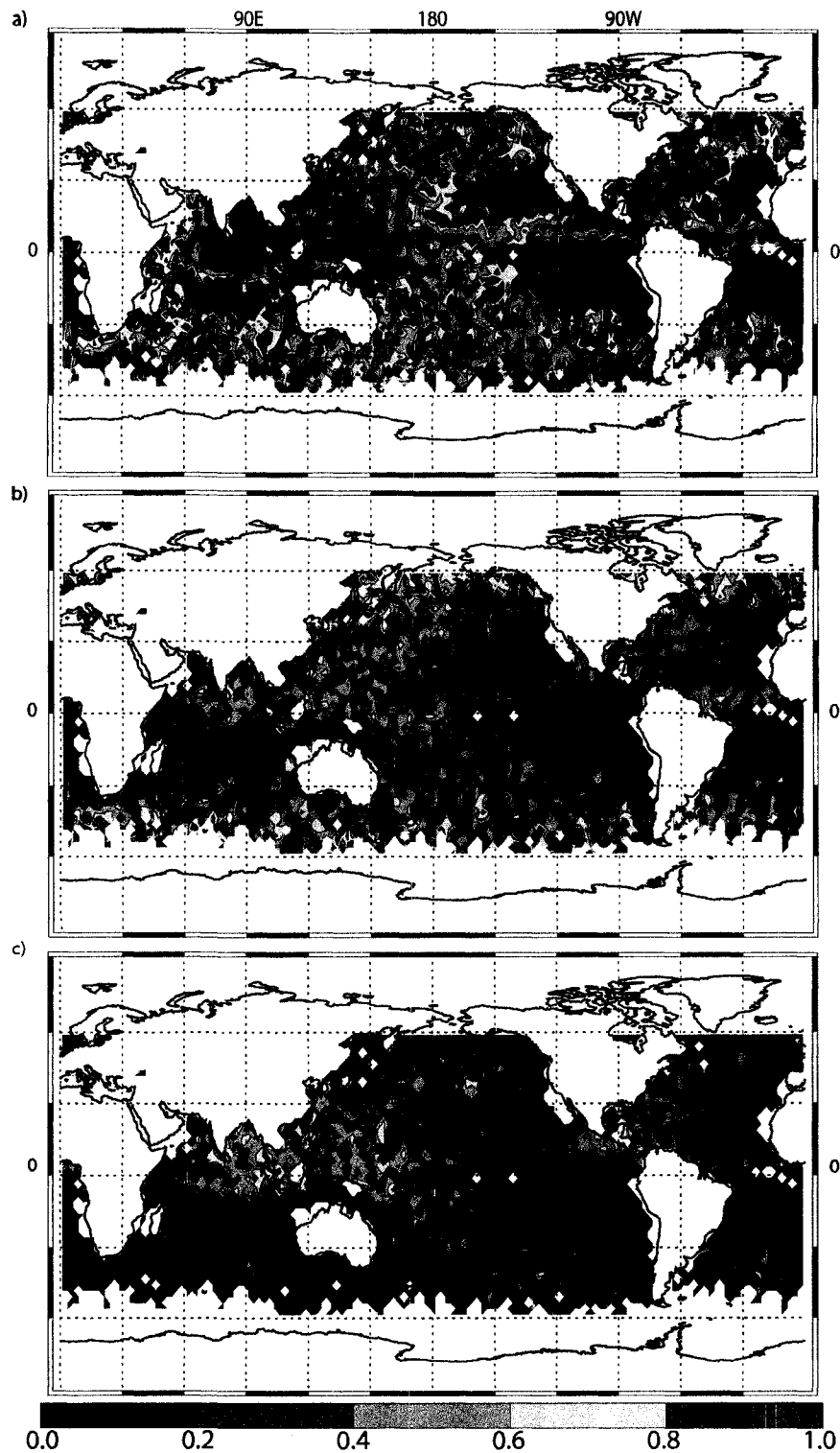


Figure 3.4: The CloudSat observed relative frequency of occurrence of the cloud height of the lowest cloud layer when precipitation is detected (CTL) in June–August 2007, broken down by three ranges of heights: (a) low clouds (less than 4.75 km), (b) mid-level clouds (between 4.75 km and 11 km), and (c) high clouds (greater than 11 km). The deepest shade of red indicates a frequency of 1.0.

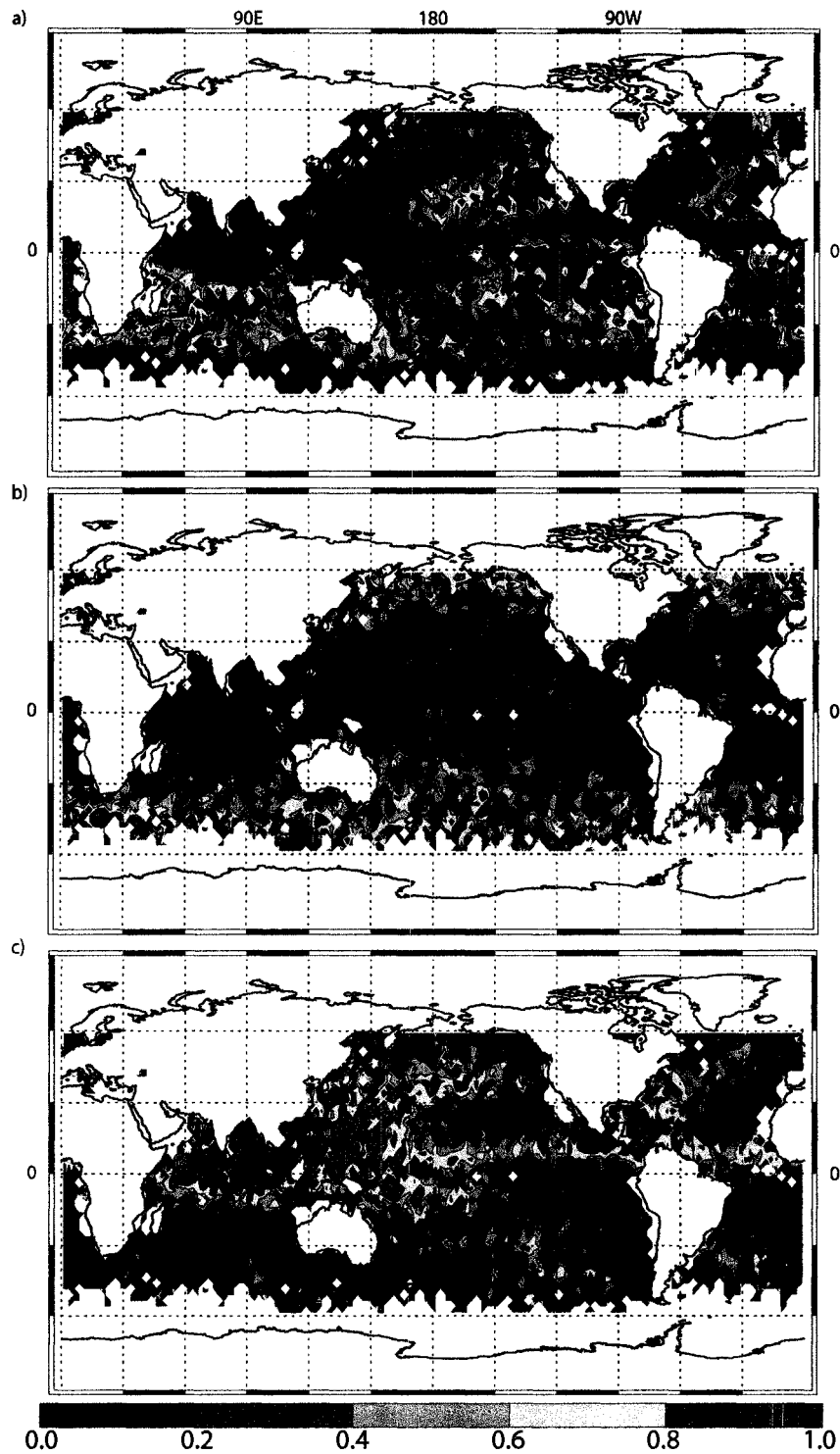


Figure 3.5: The CloudSat observed relative frequency of occurrence of the cloud height of the highest cloud layer when precipitation is detected (CTH) in June–August 2007, broken down by three ranges of heights: (a) low clouds (less than 4.75 km), (b) mid-level clouds (between 4.75 km and 11 km), and (c) high clouds (greater than 11 km). The deepest shade of red indicates a frequency of 1.0.

Figure 3.5 illustrates the often layered nature of the precipitation systems observed in the atmosphere. While Figure 3.5a demonstrates that the marine stratocumulus are often the only clouds in the sky in those regions, which is entirely consistent with the general circulation model of the ocean-atmosphere system, Figure 3.5c illustrates how high cloud pervades much of the deep tropics. These high clouds, often produced as the anvil cirrus outflow from deep convection, exist in the tropical west Pacific ocean nearly 100% of the time that precipitation is detected. One might contend that a reporting system that only reports the presence of this highest cloud top would miss the important structure of the mid-level clouds known to be precipitating beneath. A similar phenomenon occurs in the high latitudes, although in this case, more mid-level CTH is reported than mid-level CTL, indicating that shallow low clouds are precipitating underneath mid-level clouds. Perhaps this might be an indicator of a “seeder-feeder” mechanism whereby enhanced precipitation is produced when ice-crystals from a higher cloud precipitate into a lower liquid water cloud [e.g. Rutledge and Hobbs 1983], however more detailed study would be warranted before such a hypothesis could be conclusively verified. Nevertheless, the findings presented in Figures 3.4 and 3.5 confirm and expand upon the results of Haynes and Stephens [2007] which were conducted using only three months of data from early CloudSat results, and continue to be broadly consistent with the surface observations described by Stephens and Wood [2007].

### 3.3.3 CloudSat and Model Comparison Study

The CloudSat precipitation incidence results also provide a strong basis of comparison against the two special model runs provided especially for this study. The results of these comparisons are partly summarized by Figure 3.6, which presents the relative frequencies of occurrence of low, middle and high cloud top heights for likely-precipitating clouds (Figure 3.6a) and the top-most cloud in a precipitating scene (Figure 3.6b). These results include observed precipitation from CloudSat for June-August 2007, ECMWF model predictions for the same time period, and a 5 year JJA climatology from the HadGAM1 climate model. Before discussing the results, there are three procedural points are worth noting. First, because the HadGAM1 results represent a climatological average over 5 successive JJA periods, the results are greatly smoothed and many small spatial and temporal scale events will likely be averaged out of the results. Secondly, the results are broken into various regions based on latitude and longitude. Table 3.2 provides the defining coordinates for the bounding boxes for these regions, as well as various measures of the precipitation incidence in each region. Finally, for the sake of convenience, the cloud top height of the lowest cloud layer (i.e. the minimum cloud layer of the HadGAM1 model or the cloud top as calculated using the precipitation method from ECMWF) shall be referred to as the CTL to be consistent with the CloudSat nomenclature. Similarly, the cloud top height of the highest cloud top layer shall be referred to henceforth as CTH. This is not, however, meant to dismiss the differences in how these heights are calculated, but simply to connect the most similar data for simpler comparison.

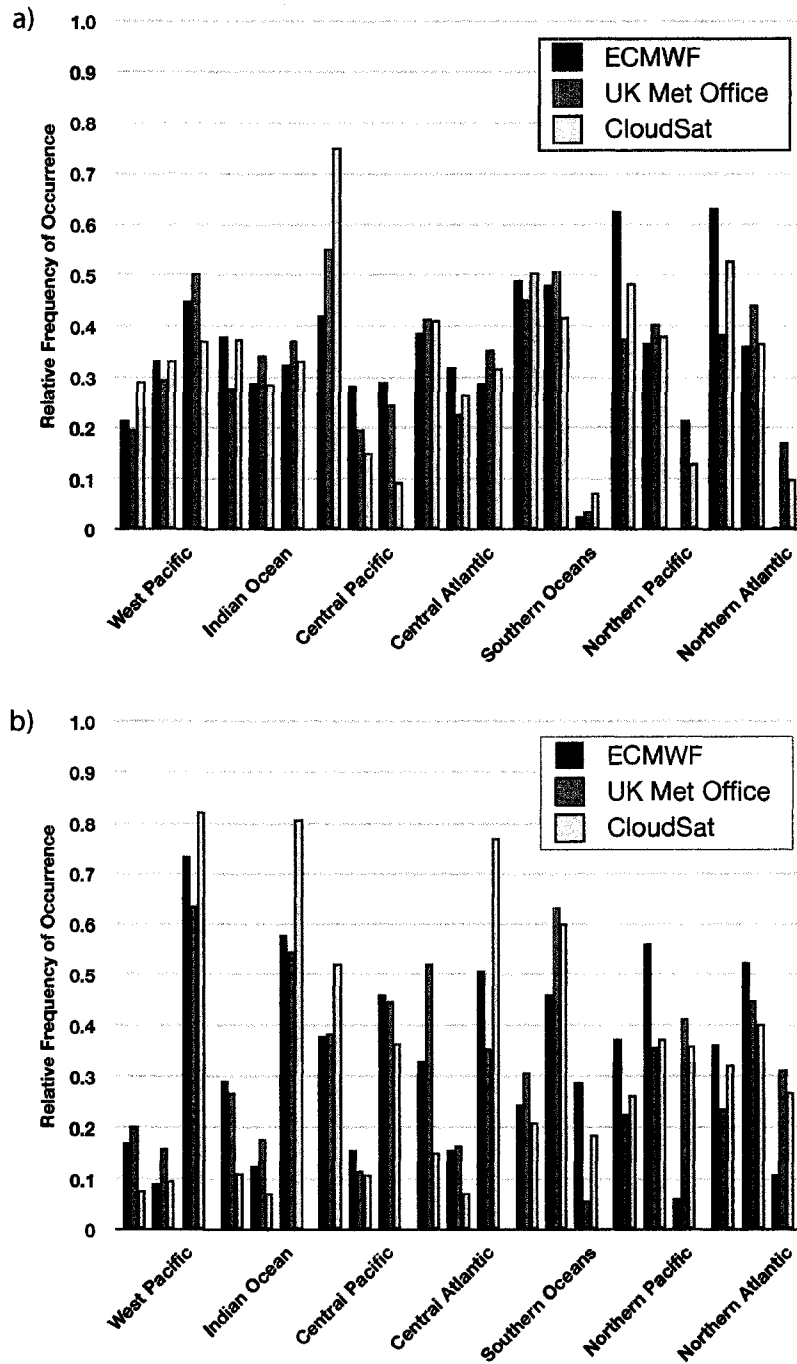


Figure 3.6: Regional breakdown of the relative frequency of occurrence of different cloud top heights for precipitation scenes. The left most set of bars represents the fraction of clouds below 4.75 km (low clouds), the middle set of bars represents the mid-level cloud top heights (4.75–11 km), and the right most set of bars represents high cloud top heights (above 11 km). In each set, the different shades distinguish between the CloudSat observed clouds and the ECMWF and HadGAM1 predict cloud distributions. The regions are defined in Table 3.2. (a) The relative frequency of cloud top height of the lowest detected cloud (CTL), which is presumably the cloud producing the surface precipitation. (b) The relative frequency of occurrence of the highest cloud top in the area (CTH). See text for more discussion.

Region	Latitudes	Longitude	CloudSat PI	HadGAM1 PI	ECMWF PI
West Pacific	10°S-20°N	105°E-160°E	0.102	0.280	0.108
Indian Ocean	10°S-30°N	95°E-105°E	0.102	0.235	0.107
Central Pacific	10°S-30°N	180°-90°W	0.182	0.174	0.060
Central Atlantic	10°S-30°N	90°W-10°E	0.164	0.174	0.111
Southern Oceans	60°S-40°S	All	0.172	0.403	0.029
Northern Pacific	30°N-60°N	140°E-120°W	0.105	0.230	0.113
Northern Atlantic	30°N-60°N	75°W-10°E	0.085	0.182	0.100

Table 3.2: Selected regions for comparison as well as observed and predicted values of precipitation incidence (PI) for each region and platform.

Figure 3.6a illustrates that there is a surprising amount of agreement between the two models and the CloudSat observations when considering the regional average statistics of the presumably precipitating clouds. In five of the seven regions, the model predicted cloud was within 10% of the observed relative frequency of occurrence. That is remarkable similarity, and somewhat unexpected when considering that these models are too spatially and temporally coarse to explicitly resolve convection. However, there are notable anomalies apparent in Figure 3.6a as well. In the Western Pacific region, both models predict about 10% more CTL classified as high cloud than CloudSat observed, which presumably means 10% more deep convection instead of shallow or congestus-mode precipitation. Meanwhile, in the Central Pacific, the ECMWF model predicts more than 30% fewer low precipitating clouds as compared to CloudSat, and the HadGAM1 model predicts 20% fewer. This finding is significant because of the important role that shallow convection plays in regulating the tropical hydrological cycle [e.g. Stephens et al., 2004]. And in the northern oceans, the ECMWF model produces no high precipitating cloud at all, which indicates that deep convection is entirely suppressed in

the midlatitudes in this model. These widely varying discrepancies in the regional average results do not however appear to support any general conclusions about the performance of the models in specific or together, excepting perhaps a suggestion that the convective parameterizations might need adjustment if the proportions of rain associated with various types of convection are incorrect.

The results of the highest cloud top heights shown in Figure 3.6b suggest much less agreement. On one hand, the agreement between the HadGAM1 climate model and CloudSat about the relative frequency of occurrence of clouds in the northern oceans is very good and the ECMWF model is not much worse, though it seems to underpredict the presence of high cloud. This suggests perhaps that the models are performing well at producing the structure of midlatitude cyclones, which CloudSat also has recently been shown to discern well [Posselt et al., 2008]. On the other hand, there is evidence that the models underdetermine the presence of high cloud over precipitating scenes in the tropics. Particularly, the predominance of high clouds in CTH observed in the tropics by CloudSat coupled with the absence of high cloud in CTL in the same locales (Figure 3.6a) suggests that these high clouds are cirrus anvils. That the models predict the presence of these clouds, up to 20-40% too infrequently in the Indian Ocean, is an issue that cannot be overstated. This study has the advantage of having been provided additional non-standard cloud layer data that allow for the identification of these layered cloud regimes. Without such additional information, there is a very high likelihood that such layered clouds could be misclassified as deep convection or perhaps thick stratocumulus –anything but the layered clouds they are. This would greatly impact the

vertical distribution of latent heating, which in turn would have consequent impacts on the general circulation of the atmosphere. This study is a unique opportunity to identify this issue and begin to study the possible effects it may have on predictions.

Another potential impact could be on the radiation budget of the models. Cirrus clouds raise the effective emission level to space. The presence of thin cirrus cloud, therefore, reduces the amount of energy emitted from the atmosphere while often negligibly reducing the solar energy input [e.g. Stephens 2005]. The effect is a net warming of the atmospheric column, which in turn has implications for the entire climate system, including the moisture budget and the general circulation of the atmosphere. As was shown in the previous chapter, the amount of atmospheric cooling is a vital cog in the machinery of precipitation prediction with respect to climate change. The lower amount of cirrus apparent in these models, particularly the climate model, is a particularly large red flag.

While the regional averages tell part of the story, they also somewhat understate some of the differences between the models' performance and the CloudSat observations. Figure 3.7 shows maps of the low, middle, and high CTL cloud top heights for the ECMWF model, and Figure 3.8 presents the same for the HadGAM1 model.

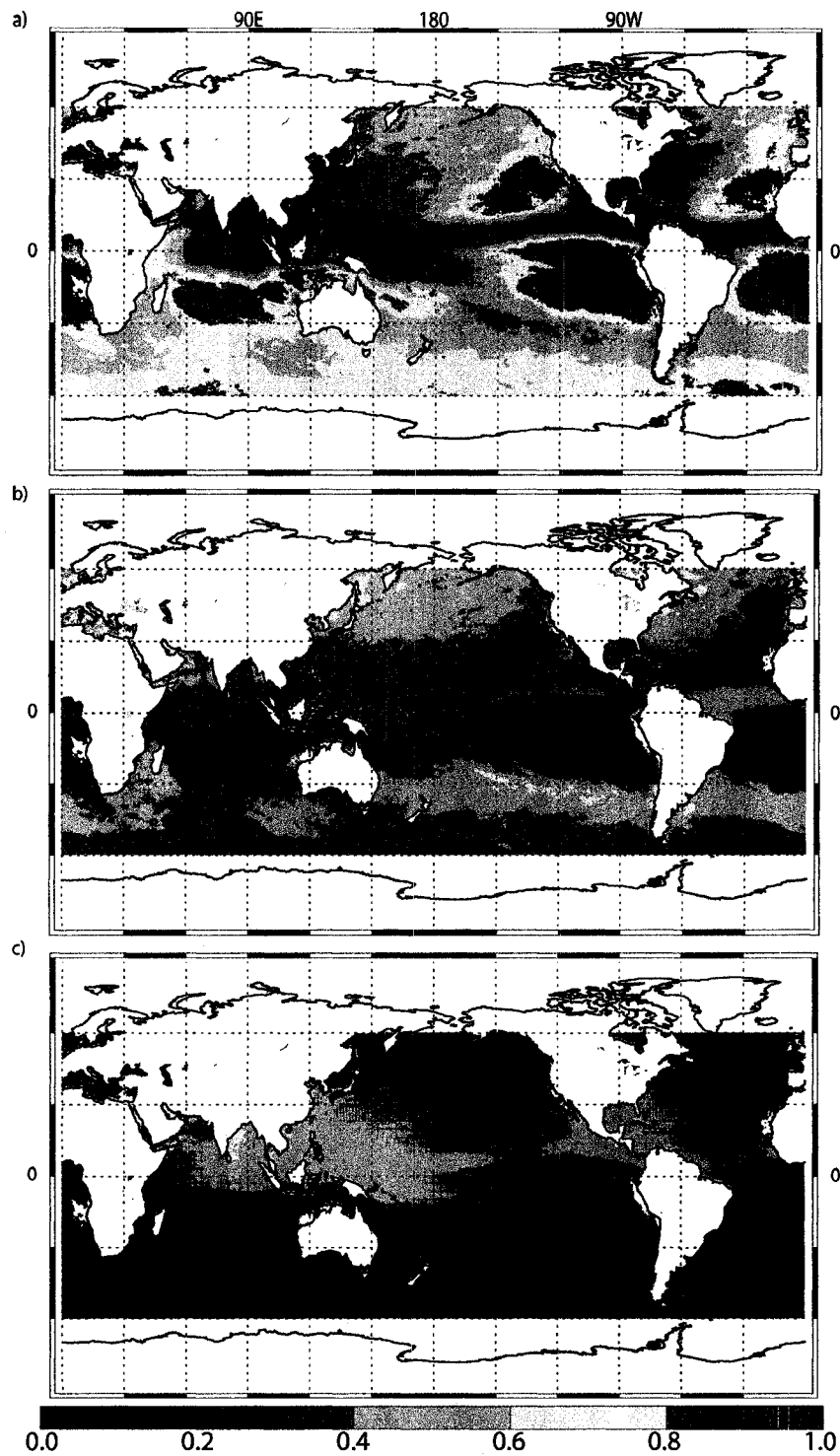


Figure 3.7: The ECMWF predicted relative frequency of occurrence of the cloud height of the lowest cloud layer when precipitation is detected (CTL) broken down by three ranges of heights: (a) low clouds (less than 4.75 km), (b) mid-level clouds (between 4.75 km and 11 km), and (c) high clouds (greater than 11 km). The deepest red shade indicates a frequency of 1.0.

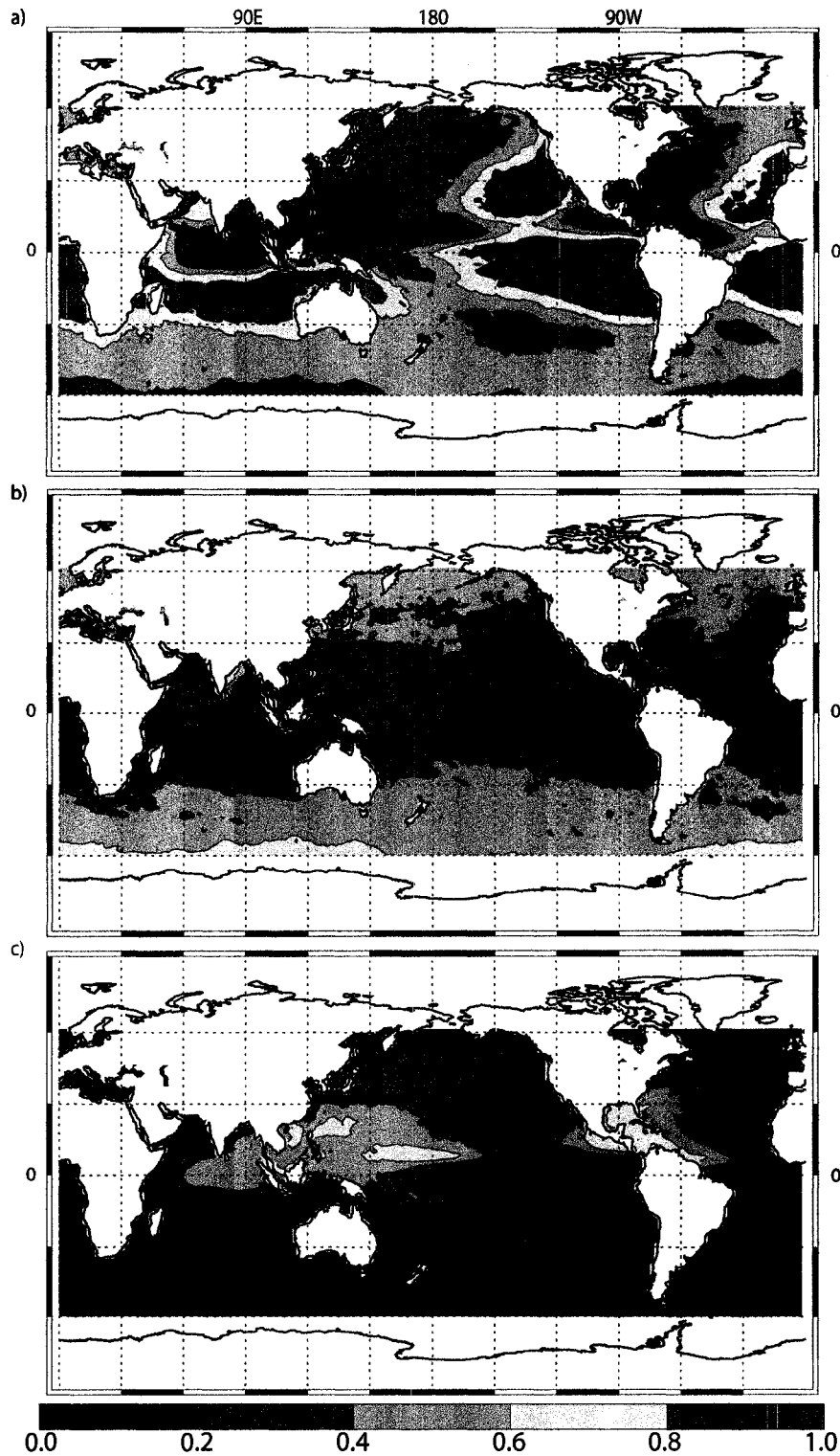


Figure 3.8: The HadGAM1 predicted relative frequency of occurrence of the cloud height of the lowest cloud layer when precipitation is detected (CTL) broken down by three ranges of heights: (a) low clouds (less than 4.75 km), (b) mid-level clouds (between 4.75 km and 11 km), and (c) high clouds (greater than 11 km). The deepest red shade indicates a frequency of 1.0.

Notably, the prevalence of low cloud in both models is much more apparent, both in areal extent and in the case of the ECMWF model, the frequency with which 100% of the precipitation is falling from low clouds. The underprediction of precipitating mid-level cloud in the tropics compared to the CloudSat observations (Figure 3.5b) is also apparent in both models. Figures 3.9 and 3.10 present similar maps, but for the highest cloud top heights. A brief comparison of the areal extent of CloudSat high cloud CTH (Figure 3.5c) to the two models (Figures 3.9c and 3.10c) reveals that the areal extent of the high cloud in the tropics predicted by the models is far less than observed. This is further evidence that the discrepancy in high cloud is likely due to underprediction of cirrus anvil clouds from deep convection in the tropics.

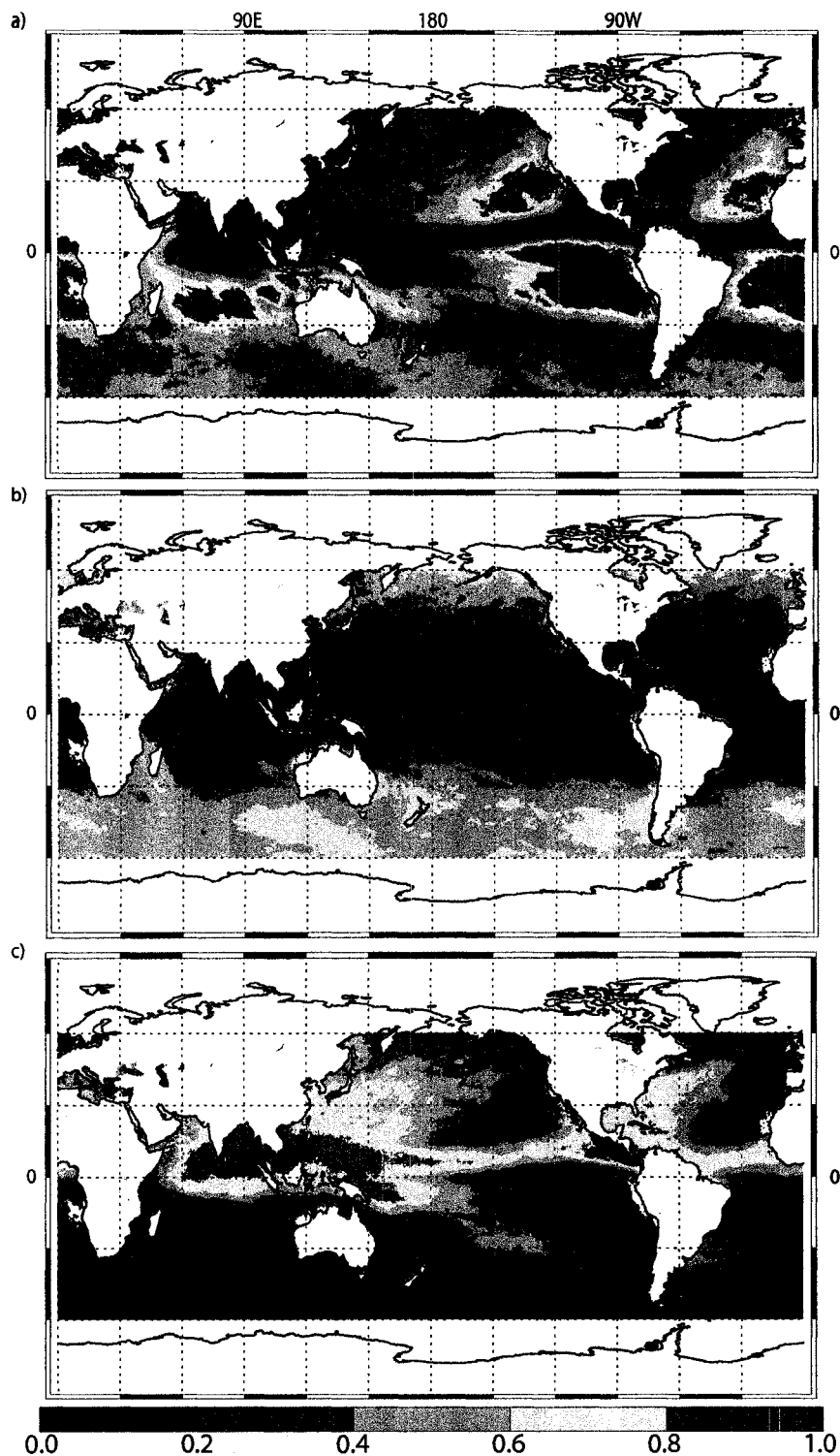


Figure 3.9: The ECMWF predicted relative frequency of occurrence of the cloud height of the highest cloud layer when precipitation is detected (CTH) broken down by three ranges of heights: (a) low clouds (less than 4.75 km), (b) mid-level clouds (between 4.75 km and 11 km), and (c) high clouds (greater than 11 km). The deepest shade of red indicates a frequency of 1.0.

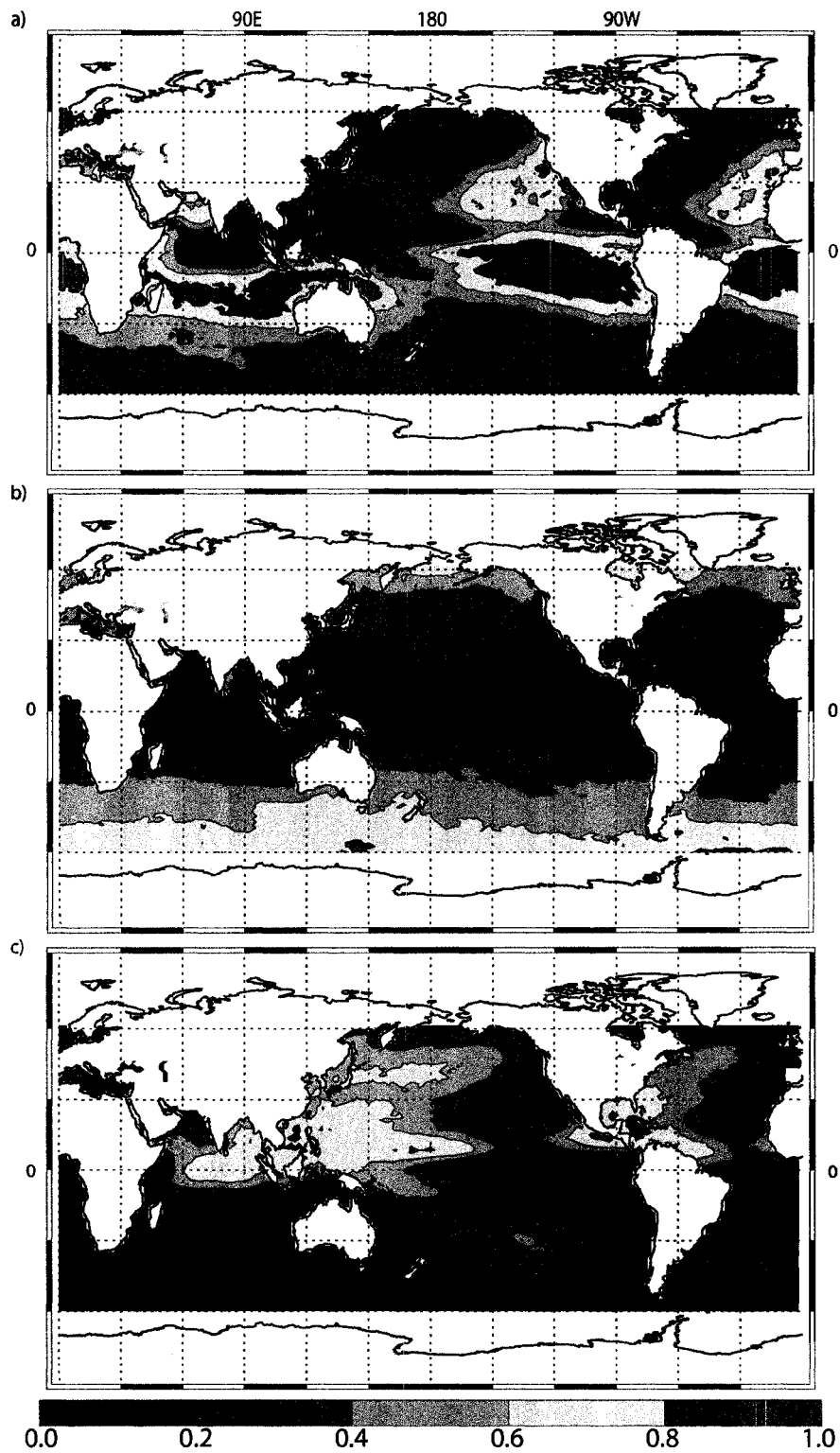


Figure 3.10: The HadGAM1 predicted relative frequency of occurrence of the cloud height of the highest cloud layer when precipitation is detected (CTH) broken down by three ranges of heights: (a) low clouds (less than 4.75 km), (b) mid-level clouds (between 4.75 km and 11 km), and (c) high clouds (greater than 11 km). The deepest shade of red indicates a frequency of 1.0.

Finally, it is important to revisit the total precipitation incidence as calculated by CloudSat and the two models. On top of all of the proportional differences in the types of clouds that produce rain, it is extremely important to keep in mind that the models produce rain with different frequencies than those observed by CloudSat. Table 3.2 illustrates that for each region, the HadGAM1 climate model produces precipitation often twice as frequently as is observed in the present climate. Meanwhile, the ECMWF model produces precipitation with nearly the same frequency, though it produces precipitation less frequently in the central Pacific and Atlantic oceans which may be connected to the differences in observed shallow convection. Given the CloudSat precipitation incidence statistics have been validated by two independent datasets in this study, one must conclude that above all, the models are likely incorrect in how often they produce precipitation.

Figure 3.11 further illustrates this point by comparing the precipitation incidence from June–August 2007 from CloudSat to the ECMWF and HadGAM1 model precipitation incidence. First of all, it must be immediately noted that each figure is plotted on a different color scale in order to call out details. The apparent differences in precipitation between the three are truly striking. The HadGAM1 model predicts many of the same spatial patterns of precipitation incidence, but with twice to three times the amplitude. The ECMWF model also retrieves some of the same patterns in the tropics, but not in the extratropics, and especially not in the northern hemisphere. Finally, if one uses the model data to calculate total precipitation incidence fraction, the ECMWF model produces precipitation 7.5% of the time, while the HadGAM1 model produces

precipitation 24.4% of the time. These values are clearly different from those observed by CloudSat, and the explanations for the differences are very obviously different for each model.

There is one final, but important caveat that must be called out in this comparison. The grid size of the models in fact play an important role in determining how frequently precipitation meets the occurrence threshold. With a larger grid size in observations or models, often the average precipitation rate is lower in order to ensure that the total precipitation for the model is consistent with the global energy budget. Therefore, a model with a larger grid size is likely to have more frequent precipitation in order to make sure the total precipitation produced still conforms to the energy budget. An example of this effect is provided by the Non-Icosahedral Atmospheric Model (NICAM). In global ocean-only precipitation incidence data provided for comparison to the results of this study [K. Suzuki, personal communication], the precipitation incidence changed from 19.6% to 18.8% when the grid size changed from 14 km to 7 km. In light of this, it is probable that some of the differences between the models and the CloudSat observations can be attributed to the scale difference between the different platforms. It may be possible to mitigate this effect by first averaging the rain rates of the platforms up to a common grid size and then determining the precipitation incidence, although this certainly would cause a loss of some of the detailed information that the fine grid scale provides. In light of this, it is clear that further study is required to understand how significantly the differing grid scales affect the results of this comparison. Nevertheless, it is expected that any effect due to this grid spacing issue would bias the results in one

direction only. Thus, this study continues to illustrate that there are significant differences between the models themselves and between the models and satellite observations. However, this study shows that these new data from CloudSat can certainly begin to unravel some of the issues at play.

### **3.4 Concluding remarks**

CloudSat radar observations of the frequency of precipitation incidence over the oceans for a period spanning August 2006 – July 2007 compare favorably to concurrent ship based and island based station observations and show a number of interesting features about the global distribution of the incidence of rain and snow. These results provide a new path for understanding how often it rains, and in this study, are used to evaluate model predictions of precipitation incidence and the types of clouds that produce that precipitation over the global oceans. Specifically, the results of this study reveal a number of promising findings:

(i) The most conservative measures of both the annual mean and the seasonal cycle of the zonal-mean frequency of precipitation occurrence from CloudSat fall within a range of values from the ICOADS dataset that are believed to represent precipitation events that may be detectable from space (Figure 3.1);

(ii) CloudSat observations of precipitation are in agreement with ship based observations well into the high latitudes, which indicates that it will provide a unique satellite-based observation of these precipitation events for the first time (Figure 3.1);

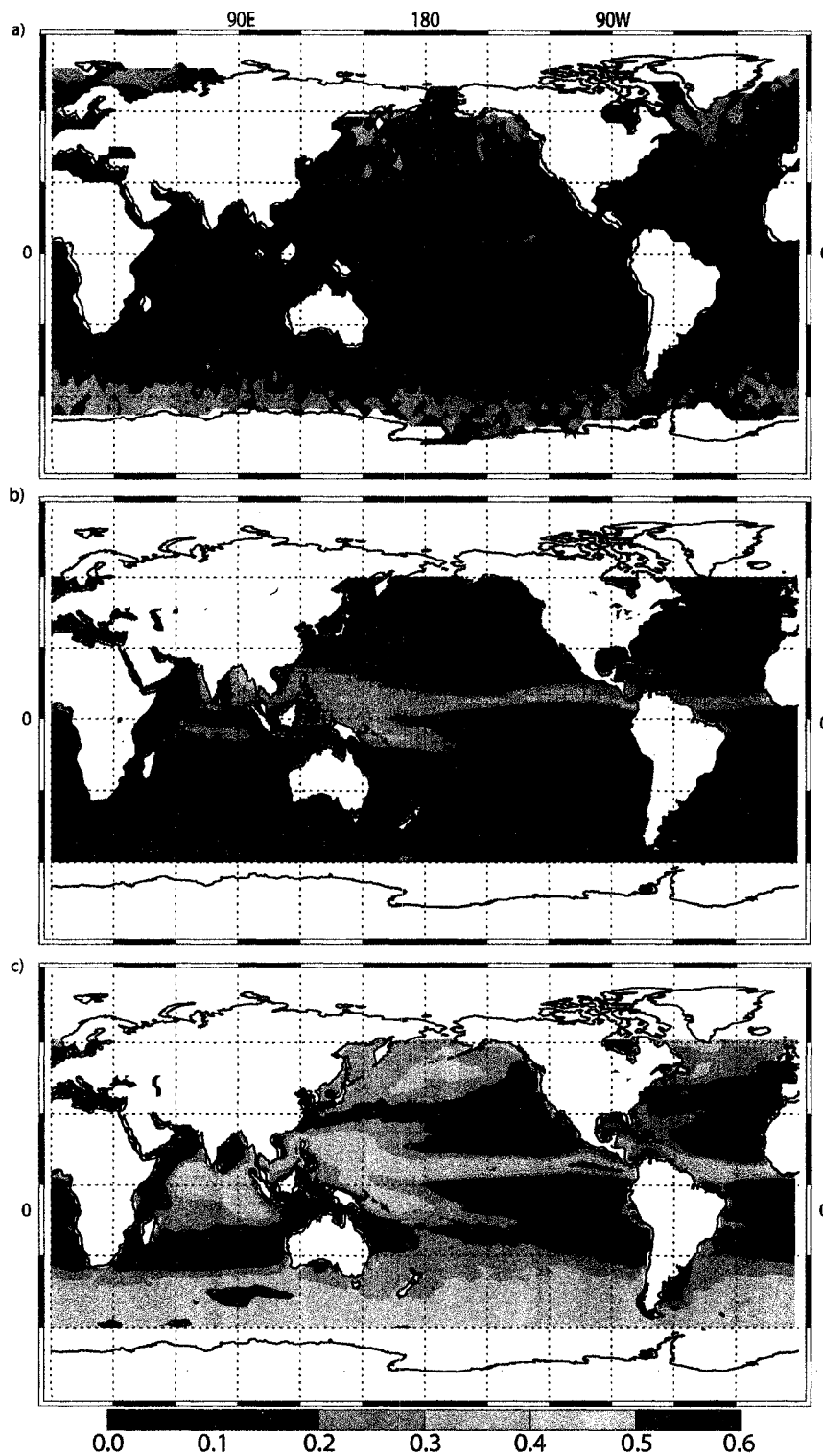


Figure 3.11: A comparison of the global maps of precipitation incidence from the three platforms used in this study. (a) The precipitation incidence from July–August 2007 as observed by CloudSat (also Figure 3.3a); (b) The precipitation incidence from July–August 2007 as predicted by the ECMWF IFS; (c) The precipitation incidence as averaged over 5 consecutive JJA seasons by the HadGAM1 climate model.

(iii) A comparison of the number of rainy days as calculated from island station data to the number of rainy days as calculated in a 2.5 x 2.5 degree box around the station from CloudSat observations show remarkable agreement despite the apparent difficulties of comparing point data to an entire grid square average (Figure 3.2);

(iv) CloudSat observations produce a near-global distribution of precipitation incidence (Figure 3.3) as well as an indication of the seasonality of the incidence of precipitation (Figure 3.4). The data indicate that precipitation occurs with 11.2% frequency in the annual mean, and that much of the precipitation that occurs poleward of 40 degrees latitude is frozen.

(v) CloudSat observations reveal the importance of mid-level clouds (between 4.75 and 11 km cloud top height) in producing precipitation in the tropics by showing that they are the lowest cloud 30% of the time it rains. They also reveal the ubiquitous nature of high level clouds layered over lower precipitating clouds in the tropics. For example, during the period from June–August 2007, there was high cloud present in the tropical West Pacific over 82% of the time. But only 37% of the time did CloudSat determine that the lowest cloud was also a high cloud, which would be an indication that a single deep convective cell was producing the rainfall. Thus, a remarkable 45% of all rainy scenes in this region consisted of a lower raining cloud overtopped by a cloud with a high cloud top (Figures 3.5, 3.6).

(vi) Special runs of the ECMWF weather forecast model and the HadGAM1 climate model were provided with additional information about the vertical profile of clouds associated with precipitation. These results were compared with the

aforementioned CloudSat observations as a means of evaluating the precipitation incidence calculated by these models (Figure 3.6–3.10). The models reproduced the heights of the lowest (presumably precipitating) clouds fairly well, particularly over extratropical regions, but serious shortcomings were identified as well. The three most important of these are that the models produce with much different frequency that that observed by CloudSat, the ECMWF model in particular fails to produce shallow precipitation in the central Pacific ocean, and both models fail to reproduce the distribution of high cloud over lower precipitating cloud. However, the different grid sizes used for each of these models and the observations may have influenced the results somewhat. Still, the implications of these results are far reaching. In addition to the obvious importance for the prediction of precipitation, the vertical structure of clouds in precipitating scenes impacts the radiative cooling of the atmosphere. As was demonstrated in the previous chapter, the radiative cooling of the atmospheric column is the important determinant for predicting the increase of global-mean precipitation caused by human-induced climate change. Therefore, it is particularly important, especially in the case of the HadGAM1 climate model, that the processes that govern the distribution of these layered cloud systems be further studied and adjusted as necessary.

# Chapter 4: Conclusions and Future Work

## 4.1 Summary of Conclusions

The overarching theme of this research is the study of precipitation. Climate models generally predict increases in precipitation of 2-3%  $\text{K}^{-1}$  of surface warming, but this increase is less than the predicted 7%  $\text{K}^{-1}$  increase of atmospheric water vapor because of the balance required between latent heating from precipitation and the clear-sky atmospheric column energy loss from increasing tropospheric water vapor due to warming. However, there are important effects that appear in the climate models due to small changes in relative humidity that are related to subtle changes in circulation or upper tropospheric absolute humidity. Clouds in these models are shown to have both positive and negative impacts on the amount of increased water vapor that can be converted into precipitation, which underscores the importance of proper cloud modeling in these climate change models.

That these theoretical and model results seemingly contradict some recent observational studies suggesting a much greater increase in precipitation rate implies issues with the satellite-based observations, not the climate predictions governed by radiative controls. To that end, this study also presents and validates precipitation incidence over the global oceans from the new precipitation dataset [Haynes et al., 2008] derived from the CloudSat Cloud Profiling Radar. These new data show that it

precipitates approximately 11% of the time in the annual mean over the oceans, and prove extremely effective at identifying both rain and snow into the high latitudes. Comparisons of these data with specially provided runs state-of-the-art climate (HadGAM1) and weather forecast (ECMWF) models provide a unique opportunity to show that both models do not accurately predict the occurrence of rainfall and do not reproduce the layered structures of raining shallow and mid-level clouds under high clouds that are prevalent over the tropical oceans.

Above all, this study underscores some parts of the extremely complex relationship between clouds and precipitation that are not yet well understood. Clouds have an obvious role in the production of precipitation, and yet the processes that lead to precipitation formation are different everywhere. The results of this study show clearly that the formation of precipitation is not well handled by models, and this must be rectified if there is hope of studying absolute quantitative predictions of precipitation changes due to climate change. Furthermore, clouds have a vital role in governing the energy balance of the planet, which in turn regulate changes in precipitation beyond simply being the birthplace of rain and snow. Measuring the radiative properties of clouds and their relationship with precipitation is an important part of the CloudSat mission. Incorporating these results into the next generation of weather and climate prediction will be an extremely important step toward achieving a better understanding of how precipitation will change in the future.

## 4.2 Questions for Future Study

Throughout the process of conducting this research, the results have raised additional questions that, while beyond the scope of this project, are certainly worthy of further analysis. The following is a brief list of some of the more interesting research questions that follow on the results of this study:

- **What are the characteristics of precipitation intensity as observed by CloudSat?**

The other half of understanding the nature of precipitation in the current climate is understanding the distribution of rainfall intensity as observed by the new CloudSat precipitation algorithm. This is a much more complicated problem than detection of precipitation, as the measurement of intensity requires accounting for the effects of multiple phases of precipitation, multiple scattering from raindrops and snowflakes, and the effects of precipitation intensity of attenuation themselves [Haynes et al., 2008]. Furthermore, at this time, it is not yet possible to determine the precipitation rate when CloudSat detects an all snow scene, making measurements of precipitation rates in the high latitudes difficult as well.

Validation will again be an important issue to resolve for these data. Petty [1995] and Dai [2001a] provide classifications of ICOADS weather codes that correspond to qualitative intensities of precipitation, but they are not quantitative, meaning that one observer's moderate rain might be another's drizzle. GSOD data provide daily accumulated precipitation which would likely be useful for performing seasonal and annual comparisons, but another independent surface-based data source is probably

needed. Higher temporal frequency data would be ideal in order to validate short-duration rainfall retrievals, but these data are often not as thoroughly quality controlled and are rarely available from surface-based data. And yet, validation of both short-term intensity and longer-duration accumulations is important. Therefore, identifying appropriate datasets for this validation remains the key issue.

- **How do state-of-the-art weather and climate models reproduce the observed intensity of precipitation in the current climate?**

Once the precipitation intensity product can be adequately identified, it can be used much as it was in this study to evaluate the relative frequency of clouds that produce various intensities of precipitation. Both the HadGAM1 climate model data and ECMWF weather model data used in Chapter 3 also provided precipitation intensity data broken down by cloud top heights of the lowest (presumably precipitating) clouds and the highest clouds in the grid box (the traditional cloud top height). These data coupled with the CloudSat intensity data will perhaps open the door to understanding why these models produce rain so often by identifying the rain processes at play. Specifically, it is especially important to understand how much precipitation is being produced shallow clouds, congestus convection, and deep convection. Each of these types of precipitation has a different latent heating profile, and therefore a different impact on both the general circulation of the atmosphere and the radiative budget of the atmosphere. If, for example, a model were producing half as much precipitation from the deep convective mode in the tropics as is observed in the environment, this reduced source of latent heating would have a drastic effect on the energy transport associated with the Walker-Hadley

circulation, including both momentum and moisture transport. This could, perhaps, be an explanation for the reduced presence of layered cirrus clouds over raining scenes in the models exhibited in this study. Comparing the intensity of models to observations may help to shed more light on results like those from the present study.

- **How do changes in the general circulation of the atmosphere relate to the regional distribution of changes to precipitation ?**

Finally, while it is vital to understand the overarching control of global-mean changes in precipitation, it is equally important to explore how precipitation changes vary regionally and the possible mechanisms behind those changes. Regional changes in precipitation arguably have a more substantial human impact, since these changes highlight geographical areas that would be predicted to see the effects of changes in storm intensity or frequency of precipitation (which in the extreme might be tied to predictions of flooding and/or drought). Moreover, the nature of the predicted regional changes provide the details that elucidate mechanisms through which global-mean changes in frequency and intensity of precipitation occur, including changes in the dynamical and thermodynamical structure of the troposphere. Therefore, in order to gain a more complete understanding of predicted changes in the global-mean climate, the regional manifestations of these changes must also be studied.

Previous studies on regional changes in precipitation give some indications of how they might be occurring in general circulation models of climate change. Model predictions of precipitation indicate both an increase in tropical precipitation and in the zonal bands associated with mid-latitude baroclinic storms [e.g. Vecchi and Soden, 2007;

Dai 2006; Sun et al., 2007]. The changes in tropical precipitation have been ascribed to be related to changes in the tropical Walker circulation and associated vertical atmospheric motions [Vecchi and Soden, 2007; Held and Soden, 2006]. Changes in precipitation in the extra-tropics might be expected to be related to changes in the meridional temperature gradient, which is generally predicted to decrease due to accelerated warming in the polar regions [Trenberth et al., 2007b]. Yet, it is apparent from the aforementioned studies that both total precipitation and convective precipitation is increasing in the mid-latitudes. A different approach appears to be necessary to understand why this apparent discrepancy exists.

The study of the energetics of general circulation of the atmosphere conducted by Lorenz [1955] provides a useful method for gaining additional insights as to how the atmospheric circulation may be changing in climate change scenarios. In this study, Lorenz partitions the total available energy of the atmosphere into four distinct parts: zonal kinetic energy (KZ), zonal available potential energy (AZ), eddy kinetic energy (KE), and eddy available potential energy (AE). These partitions represent the motions of the atmosphere and the amount of total (gravitational plus internal) potential energy available for those motions. The generation, conversion, and dissipation of energy from these reservoirs represent processes, including baroclinic midlatitude eddies and changes in the Walker circulation, that describe the basic energy cycle of the atmosphere. The changes in the atmospheric radiative budget that lead to global warming must be related to changes in these energy reservoirs and the processes that describe their sources and

sinks. Therefore, the nature of changes in these energetics should illuminate the pattern of regional changes in precipitation intensity and frequency.

The extratropical patterns of precipitation changes can also be elucidated by examining changes in the tracks of midlatitude baroclinic cyclones. Recent observational studies surveyed by Trenberth et al. [2007b] indicate that storm tracks have changed over the past few decades [see McCabe et al., 2001 and Wang et al., 2006 among others]. Changes in the storm tracks, defined by Trenberth [1991] as regions of maximum variance in middle and upper tropospheric geopotential heights, would necessarily tie in with the Lorenz energy cycles as described above. However, a systematic study of storm tracks in the general circulation models, along the vein of observational study of Trenberth [1991] that applied a 2- to 8-day bandpass filter to data to isolate these phenomena, would provide additional corroborating information about the structure of these storms and their relation to the changes in the atmospheric energy cycle.

## Chapter 5: Bibliography

- Allan, R. P., and B. J. Soden (2007), Large discrepancy between observed and simulated precipitation trends in the ascending and descending branches of the tropical circulation, *Geophys. Res. Lett.*, *34*, L18705, doi:10.1029/2007GL031460.
- Allen, M. A., and W. J. Ingram (2002), Constraints on future changes in climate and the hydrologic cycle, *Nature*, *419*, 224–232, doi:10.1038/nature01092.
- Berg, W., T. L'Ecuyer, and C. Kummerow (2006), Rainfall climate regimes: The relationship of TRMM rainfall biases to the environment, *J. Appl. Meteorol. Clim.*, *45*, 434–454, doi:10.1175/JAM2331.1.
- Bodas-Salcedo, A., M. A. Ringer, and A. Jones (2008), Evaluation of the surface radiation budget in the atmospheric component of the Hadley Centre Global Environmental Model (HadGEM1), *J. Clim.*, doi:10.1175/2008JCLI2097.1. In Press.
- Bosilovich, M. G., S. D. Schubert, and G. K. Walker (2005), Global changes in water cycle intensity, *J. Clim.*, *18*, 1591–1608, doi:10.1175/JCLI3357.1.
- Chahine, M. T. (1992), The hydrological cycle and its influence on climate, *Nature*, *359*, 373–380, doi:10.1038/359373a0.
- Clarke, R. and J. King (2004), *The Water Atlas*, 122 pp., The New Press.
- Dai, A. (2001a), Global precipitation and thunderstorm frequencies. Part I: Seasonal and interannual variations, *J. Clim.*, *14*, 1092–1111, doi:10.1175/1520-0442(2001)014<1092:GPATFP>2.0.CO;2.

- Dai, A. (2001b), Global precipitation and thunderstorm frequencies. Part II: Diurnal variations, *J. Clim.*, *14*, 1112–1128, doi:  
10.1175/1520-0442(2001)014<1112:GPATFP>2.0.CO;2.
- Dai, A. (2006), Recent climatology, variability, and trends in global surface humidity, *J. Clim.*, *19*, 3589–3606, doi:10.1175/JCLI3816.1.
- Dai, A., I. Y. Fung, and A. D. Del Genio (1997), Surface observed global land precipitation variations during 1900–88, *J. Clim.*, *10*, 2943–2962, doi:  
10.1175/1520-0442(1997)010<2943:SOGLPV>2.0.CO;2.
- Davies, T., M. J. P. Cullen, A. J. Malcolm, M. H., Mawson, A. Staniforth, A. A. White, N. Wood (2005), A new dynamical core for the Met Office’s global and regional modelling of the atmosphere, *Q. J. R. Meteorol. Soc.*, *131*, 1759–1782, doi:  
10.1256/qj.04.101.
- Diaz, H. F., R. S. Bradley, and J. K. Eischeid (1989), Precipitation fluctuations over global land areas since the late 1800’s, *J. Geophys. Res.*, *94*(D1), 1195–1210.
- Emori, S., and S. J. Brown (2005), Dynamic and thermodynamic changes in mean and extreme precipitation under changed climate, *Geophys. Res. Lett.*, *32*, L17706, doi:10.1029/2005GL023272.
- Folland, C. K., and D. E. Parker (1995), Correction of instrumental biases in historical seas surface temperature data, *Q. J. R. Meteorol. Soc.*, *121*, 319–367, doi:10.1002/qj.49712152206.

- Frisch, A. S., C. W. Fairall, and J. B. Snider (1995), Measurement of stratus cloud and drizzle parameters in ASTEX with a K<sub>a</sub>-band Doppler radar and a microwave radiometer, *J. Atmos. Sci.*, *52*, 2788–2799, doi:10.1175/1520-0469(1995)052<2788:MOSCAD>2.0.CO;2.
- Fu, Q., C. M. Johanson, J. M. Wallace, and T. Reichler (2006), Enhanced mid-latitude tropospheric warming in satellite measurements, *Science*, *312*, 1179, doi:10.1126/science.1125566.
- Goody, R. M. (1964), *Atmospheric Radiation I*, 436 pp, Clarendon Press, Oxford.
- Goody, R. M., and Walker, J. C. G. (1972), *Atmospheres*, 150 pp., Prentice-Hall, Englewood Cliffs, New Jersey.
- Goody, R. M., and Yung, Y. L. (1995), *Atmospheric radiation: theoretical basis*, 2nd ed., 544 pp., Oxford U. P., New York.
- Groisman, P. Y., R. W. Knight, D. R. Easterling, T. R. Karl, G. C. Hegerl, and V. N. Razuvaev (2005), Trends in intense precipitation in the climate record, *J. Clim.*, *18*, 1326–1352, doi:10.1175/JCLI3339.1.
- Gu, G., R. F. Adler, G. J. Huffman, and S. Curtis (2007), Tropical rainfall variability on interannual-to-interdecadal and longer time scales derived from the GPCP monthly product, *J. Clim.*, *20*, 4033–4046, doi:10.1175/JCLI4227.1.
- Haynes, J. M., and G. L. Stephens (2007), Tropical oceanic cloudiness and the incidence of precipitation: Early results from CloudSat. *Geophys. Res. Lett.*, *34*, L09811, doi:10.1029/2007GL029335.

- Haynes, J. M., T. S. L'Ecuyer, G. L. Stephens, S. D. Miller, C. Mitrescu, N. B. Wood, and S. Tanelli (2008), Rainfall retrieval over the ocean with spaceborne W-band radar. *J. Geophys. Res.* In press.
- Held, I. M., and B. J. Soden (2000), Water vapor feedback and global warming, *Ann. Rev. Energy Environ.*, 25, 441–475, doi:10.1146/annurev.energy.25.1.441.
- Held, I. M., and B. J. Soden (2006), Robust responses of the hydrological cycle to global warming, *J. Clim.*, 19, 5686–5699, doi:10.1175/JCLI3990.1.
- Huffman, G. J., and Coauthors (1997), The Global Precipitation Climatology Project (GPCP) combined precipitation dataset, *Bull. Am. Meteorol. Soc.*, 78, 5–20, doi:10.1175/1520-0477(1997)078<0005:TGPCPG>2.0.CO;2.
- Im, E. S., L. Durden, and C. Wu (2005), Cloud profiling radar for the CloudSat mission, *IEEE Aerosp. Electron. Syst. Mag.*, 20, 15–18, doi:10.1109/RADAR.2005.1435874.
- Johnson, R. H., T. M. Rickenbach, S. A. Rutledge, P. E. Ciesielski, and W. H. Schubert (1999), Trimodal characteristics of tropical convection, *J. Clim.*, 12, 2397–2418, doi:10.1175/1520-0442(1999)012<2397:TCOTC>2.0.CO;2.
- Kharin, V. V., and F. W. Zwiers (2005), Estimating extremes in transient climate change simulations, *J. Clim.*, 18, 1156–1173, doi:10.1175/JCLI3320.1.
- Lambert, F. H., A. R. Stine, N. Y. Krakauer, and J. C. H. Chiang (2008), How much will precipitation increase with global warming?, *EOS Trans. AGU.*, 89(21), 193–194.
- Lorenz, E. N. (1955), Available potential energy and the maintenance of the general circulation, *Tellus*, 7, 157–167.

- Lott, J.N., and R. Baldwin (2002), The FCC integrated surface hourly database, a new resource of global climate data. 13th Symposium on Global Change and Climate Variations, 13-17 January 2002, Orlando, Florida, American Meteorological Society, Boston, MA, 70-72.
- Lu, J., G. Vecchi, and T. Reichler (2007), Expansion of the Hadley cell under global warming, *Geophys. Res. Lett.*, *34*, L06805, doi:10.1029/2006GL028443.
- Mace, G. G., R. Marchand, Q. Zhang, and G. Stephens (2007), Global hydrometeor occurrence as observed by CloudSat: Initial observations from summer 2006, *Geophys. Res. Lett.*, *34*, L09808, doi:10.1029/2006GL029017.
- Manabe, S., and R. F. Strickler (1964), Thermal equilibrium of the atmosphere with a convective adjustment, *J. Atmos. Sci.*, *21*, 361–385, doi: 10.1175/1520-0469(1964)021<0361:TEOTAW>2.0.CO;2.
- Mann, M. E., and P. D. Jones (2003), Global surface temperatures over the past two millenia, *Geophys. Res. Lett.*, *30*(15), 1820, doi:10:1029/2003GL017814.
- Martin, G. M., M. A. Ringer, V. D. Pope, A. Jones, C. Dearden, and T. J. Hinton (2006), The physical properties of the atmosphere in the new Hadley Centre Global Environmental Model (HadGEM1). Part I: Model description and global climatology, *J. Clim.*, *19*(7), 1274–1301, doi:10.1175/JCLI3636.1.
- McCabe, G. J., M. P. Clark, and M. C. Serreze (2001), Trends in northern hemisphere surface cyclone frequency and intensity, *J. Clim.*, *14*, 2763–2768, doi: 10.1175/1520-0442(2001)014<2763:TINHSC>2.0.CO;2.

- Meehl, G. A., J. M. Arblaster, and C. Tebaldi (2005), Understanding future patterns of increased precipitation intensity in climate model simulations, *Geophys. Res. Lett.*, *32*, L18719, doi:10.1029/2005GL023680.
- Meehl, G. A., C. Covey, T. Delworth, M. Latif, B. McAvaney, J. F. B. Mitchell, R. J. Stouffer, and K. E. Taylor (2007), The WCRP CMIP3 multimodel dataset: A new era in climate change research, *Bull. Am. Meteorol. Soc.*, *81*, 1383–1394, doi:10.1175/BAMS-88-9-1383.
- Mitchell, J. F. B., C. A. Wilson, and W. M. Cunningham (1987), On CO<sub>2</sub> climate sensitivity and the model dependence of results, *Q. J. R. Meteorol. Soc.*, *113*, 293–322, doi:10.1002/qj.49711347517.
- North, G. R., R. F. Cahalan, and J. A. Coakley, Jr. (1981), Energy balance climate models, *Rev. Geophys. Space Phys.*, *19*, 91–121.
- Pall, P., M. R. Allen, and D. A. Stone (2007), Testing the Clausius-Clapeyron constraint on changes in extreme precipitation under CO<sub>2</sub> warming, *Clim. Dyn.*, *28*, 351–363, doi:10.1007/s00382-006-0180-2.
- Petty, G. W. (1995), Frequencies and characteristics of global oceanic precipitation from shipboard present-weather reports. *Bull. Am. Meteorol. Soc.*, *76*, 1593–1616, doi:10.1175/1520-0477(1995)076<1593:FACOGO>2.0.CO;2.
- Petty, G. W. (1997), An intercomparison of oceanic precipitation frequencies from 10 special sensor microwave/imager rain rate algorithms and shipboard present weather reports, *J. Geophys. Res.*, *102*(D2), 1757–1777.

- Posselt, D. J., G. L. Stephens, and M. Miller (2008), CloudSat: Adding a new dimension to a classical view of extratropical cyclones, *Bull. Am. Meteorol. Soc.*, *89*, 599–609, doi:10.1175/BAMS-89-5-599.
- Ringer, M. A., and Coauthors (2006), The physical properties of the atmosphere in the new Hadley Centre Global Environmental Model (HadGEM1). Part II: Aspects of variability and regional climate, *J. Clim.*, *19*, 1274–1301, doi:10.1175/JCLI3713.1.
- Rutledge, S. A., and P. V. Hobbs (1983), The mesoscale and microscale structure and organization of clouds and precipitation in midlatitude cyclones. VIII: A model for the “seeder-feeder” process in warm-frontal rainbands, *J. Atmos. Sci.*, *40*, 1185–1206, doi:10.1175/1520-0469(1983)040<1185:TMAMSA>2.0.CO;2.
- Santer, B. D., and Coauthors (2007), Identification of human-induced changes in atmospheric moisture content, *Proc. Natl. Acad. Sci. USA*, *104*, 15248–15253, doi:10.1073/pnas.0702872104.
- Schiffer, R. A. and W. B. Rossow (1983), The International Satellite Cloud Climatology Project (ISCCP): The first project of the World Climate Research Programme, *Bull. Am. Meteorol. Soc.*, *64*, 779–784.
- Schumacher, C., and R. A. Houze, Jr. (2000), Comparison of radar data from the TRMM satellite and Kwajalein oceanic validation site, *J. Appl. Meteorol.*, *39*, 2151–2164, doi:10.1175/1520-0450(2001)040<2151:CORDFT>2.0.CO;2.

- Seager, R., and Coauthors (2007), Model projections of an imminent transition to a more arid climate in southwestern North America, *Science*, 316, 1181–1184, doi: 10.1126/science.1139601.
- Stephens, G. L. (1990), On the relationship between water vapor over the oceans and sea surface temperature, *J. Clim.*, 3, 634–645, doi: 10.1175/1520-0442(1990)003<0634:OTRBWV>2.0.CO;2.
- Stephens, G. L. (2005), Cloud feedbacks in the climate system: A critical review, *J. Clim.*, 18, 237–273, doi:10.1175/JCLI-3243.1.
- Stephens, G. L., and T. D. Ellis (2008), Controls of global-mean precipitation increases in global warming GCM experiments, *J. Clim.*, in press.
- Stephens, G. L., and C. D. Kummerow (2007), The remote sensing of clouds and precipitation from space: A review, *J. Atmos. Sci.*, 88, 1608–1624, doi: 10.1175/2006JAS2375.1.
- Stephens, G. L., and N. L. Wood (2007), Properties of tropical convection observed by millimeter-radar systems, *Mon. Weather Rev.*, 125, 821–842, doi:10.1175/MWR3321.1.
- Stephens, G. L., A. Slingo, M. J. Webb, P. J. Minnett, P. H. Daum, L. Kleiman, I. Wittmeyer, and D. A. Randall (1994), Observations of the Earth's radiation budget in relation to atmospheric hydrology. 4. Atmospheric column radiative cooling over the worlds' oceans, *J. Geophys. Res.*, 99(D9), 18585–18604, doi: 10.1029/94JD01151.

- Stephens, G. L., and Coauthors (2002), The CloudSat mission and the A-train, *Bull. Am. Meteorol. Soc.*, *83*, 1771–1790, doi:10.1175/BAMS-83-12-1771.
- Stephens, G. L., P. J. Webster, R. H. Johnson, R. Engelen, and T. L'Ecuyer (2004), Observational evidence for the mutual regulation of the tropical hydrological cycle and tropical sea surface temperatures, *J. Clim.*, *17*, 2213–2224, doi:10.1175/1520-0442(2004)017<2213:OEFTMR>2.0.CO;2.
- Stephens, G. L., and Coauthors (2008), The CloudSat Mission: Performance and early science after the first year of operation. Submitted to *J. Geophys. Res.*
- Stevens, B., and Coauthors (2003), Dynamics and chemistry of marine stratocumulus – DYCOMS-II, *Bull. Am. Meteorol. Soc.*, *84*, 579–593, doi:10.1175/BAMS-84-5-579.
- Sun, Y., S. Solomon, A. Dai, and R. W. Portmann (2006), How often does it rain?, *J. Clim.*, *19*, 916–934, doi:10.1175/JCLI3672.1.
- Tompkins, A.M., P. Bechtold, A.C.M. Beljaars, A. Benedetti, S. Cheinet, M. Janisková, M. Köhler, P. Lopez, and J.-J. Morcrette (2004), Moist physical processes in the IFS: Progress and Plans, ECMWF Tech Memo 452,. 91 pp.
- Trenberth, K. E. (1991), Storm tracks in the southern hemisphere, *J. Atmos. Sci.*, *48*, 707–722, doi:10.1175/1520-0442(1991)004<0707:CDFGAC>2.0.CO;2.
- Trenberth, K. E. (1998), Atmospheric moisture residence times and cycling: Implications for rainfall rates and climate change, *Climatic Change*, *39*, 667–694, doi:10.1023/A:1005319109110.

- Trenberth, K. E., A. Dai, R. M. Rasmussen, and D. B. Parsons (2003), The changing character of precipitation, *Bull. Am. Meteorol. Soc.*, *84*, 1205–1217, doi:10.1175/BAMS-84-9-1205.
- Trenberth, K. E., J. Fasullo, and L. Smith (2005), Trends and variability in column-integrated atmospheric water vapor, *Clim. Dyn.*, *24*, 741–758, doi:10.1007/s00382-005-0017-4.
- Trenberth, K. E., L. Smith, T. Qian, A. Dai, and J. Fasullo (2007a) Estimates of the global water budget and its annual cycle using observational and model data, *J. Hydrometeor.*, *8*, 758-769, doi:10.1175/JHM600.1.
- Trenberth, K. E., and Coauthors (2007b), Observations: Surface and atmospheric climate change. In: *Climate Change 2007: The Physical Science Basis*. Solomon, S., D. Qin, M. Manning, Z. Chen, M. Marquis, K. B. Averyt, M. Tignor, and H. L. Miller, Eds. 996 pp., Cambridge U. P.
- Tselioudis, G., and W. B. Rossow (2006), Climate feedback implied by observed radiation and precipitation changes with midlatitude storm strength and frequency, *Geophys. Res. Lett.*, *33*, L02704, doi:10.1029/2005GL024513.
- UNDP (United Nations Development Programme) (2007), *Human Development Report 2007: Fighting climate change: Human solidarity in a divided world*, 399 pp., Palgrave Macmillan.
- Vecchi, G. A., and B. J. Soden (2007), Global warming and the weakening of the tropical circulation, *J. Clim.*, *20*, 4316–4340, doi:10.1175/JCLI4258.1.

- Wang, X. L., V. R. Swail, and F. W. Zwiers (2006), Climatology and changes of extratropical storm tracks and cyclone activity: Comparison of ERA-40 with NCEP/NCAR Reanalysis for 1958–2001, *J. Clim.*, *19*, 3145–3166, doi:10.1175/JCLI3781.1.
- Wentz, F. J., and M. Schabel (2000), Precise climate monitoring using complementary satellite data sets, *Nature*, *403*, 414–416, doi:10.1038/35000184.
- Wentz, F. J., L. Ricciardulli, K. Hilburn, and C. Mears (2007), How much more rain will global warming bring?, *Science*, *317*, 233–235, doi:10.1126/science.1140746.
- Wilheit, T., C. Kummerow, and R. Ferraro (2003), Rainfall algorithms for AMSR-E, *IEEE Trans. Geosci. Rem. Sens.*, *41*(2), 204–214.
- Willet, K. M., N. P. Gillett, P. D. Jones, and P. W. Thorne (2007), Attribution of observed surface humidity changes to human influence, *Nature*, *449*, 710–712, doi:10.1038/nature06207.
- Worley, S. J., S. D. Woodruff, R. W. Reynolds, S. J. Lubker, and N. Lott (2005), ICOADS release 2.1 data and products. *Int. J. Climatol.* (CLIMAR-II Special Issue), *25*, 823–842, doi: 10.1002/joc.1166.
- Zhang, X., F. W. Zwiers, G. C. Hegerl, F. H. Lambert, N. P. Gillett, S. Solomon, P. A. Stott, and T. Nozawa (2007), Detection of human influence on twentieth-century precipitation trends, *Nature*, *448*, 461–465, doi:10.1038/nature06025.